https://doi.org/10.5194/egusphere-2025-3153
Preprint. Discussion started: 10 July 2025

Hydroclimate Evolution Along Chile Over the Last 20,000 Years: Insights from Leaf-Wax Hydrogen Isotope Records

Charlotte Läuchli[1], Nestor Gaviria-Lugo[2], Anne Bernhardt[1], Hella Wittmann[2], Patrick J. Frings[2], Mahyar Mohtadi[5], Andreas Lückge[6], Dirk Sachse[3,4]

[1]Institute of Geological Sciences, Freie Universität Berlin, Berlin, 12249, Germany
[2]Earth Surface Geochemistry, GFZ Helmholtz Centre for Geosciences, Potsdam, 14473, Germany
[3]Geomorphology, GFZ Helmholtz Centre for Geosciences, Potsdam, 14473, Germany
[4]Geography Department, Humboldt-Universität zu Berlin, Berlin, 10099, Germany
[5]MARUM – Center for Marine Environmental Sciences, University of Bremen, Bremen, 28359, Germany
[6]Federal Institute for Geosciences and Natural Resources (BGR), Hannover, 30655, Germany

Correspondence to: Charlotte Läuchli (laeuchli@zedat.fu-berlin.de)

Abstract. The climate of the western coast of South America is controlled by large climate systems known as the Intertropical Convergence Zone (ITCZ), the Subtropical Pacific High (SPH) and the Southern Hemisphere Westerly wind (SWW) belt. While the large-scale evolution of the SWW belt and the location of the ITCZ are well constrained, the interaction between these two climate features is not well understood as a high resolution spatial and temporal reconstruction of the SWW belt is still lacking. Here, we use the hydrogen isotope ratios of leaf-wax n-alkanes in marine sediments between 33°S and 36°S offshore Chile to reconstruct past hydrological regimes and the evolution of the SWW belt since the Last Glacial Maximum (LGM, ca. 20,000 cal yr BP). Our results suggest overall wet conditions during the LGM, followed by increasing aridity during the deglaciation period. This shift toward drier conditions was briefly interrupted during the Antarctic Cold Reversal. The early Holocene was then marked by dry conditions until ca. 7,500 cal yr BP, after which a return to wetter conditions marked latitudes south of 36°S. During the last 5,500 years, wetter conditions progressively characterized latitudes as far north as 30°S. These results reflect past changes in the latitudes of the SWW belt and imply a northward position of the SWW belt during the LGM, followed by a southward migration of the SWW belt during the deglaciation period. This shift southward was briefly interrupted during the Antarctic Cold Reversal. The SWW belt reached its southernmost latitudes during the early Holocene. At ca. 7,500 cal yr BP, a displacement northward of the SWW belt was detected at latitudes south of 36°S and during the last 5,500 years, the SWW belt progressively migrated northward. Our reconstruction, compared with past latitude of the ITCZ, shows that the climate was predominantly, but not exclusively, controlled by the El-Niño Southern Oscillation and insolation during the Holocene, while atmospheric pathways associated with large interhemispheric temperature gradient and changes in the Hadley cell circulation prevailed from 17,000 to 11,500 cal yr BP.

1 Introduction

South America is affected by large-scale climate features that shape the Earth's climate system and its evolution, particularly by the location of the Southern Westerly Wind (SWW) belt, the position and extent of the Subtropical Pacific High (SPH), and of the position and width of the Intertropical Convergence Zone (ITCZ). For example, the migration of the SWW belt located at extratropical to subpolar latitudes is suggested to affect the ventilation of the deep water of the Southern Ocean and, by doing so, impact the atmospheric CO_2 (e.g., Menviel et al., 2018; Toggweiler et al., 2006; Völker and Köhler, 2013). At tropical latitudes, the ITCZ – a minimum pressure belt characterized by intense convection corresponding to the ascending branch of the Hadley cell (e.g., Waliser and Gautier, 1993) – potentially influence the Hadley cell circulation (Watt-Meyer and Frierson, 2019) and, thus, the redistribution of moisture and heat both intra- and interhemispherically (e.g., Hadley, 1997; Watt-Meyer and Frierson, 2019). The modern components of the SWW and the ITCZ are relatively well understood (e.g., Garreaud, 2009; Garreaud et al., 2009) and several studies have investigated their past evolution (e.g., Arbuszewski et al., 2013; Haug et al., 2001b; Kaiser et al., 2024; Lamy et al., 2001; Sachs et al., 2009), yet forcing mechanisms and especially dynamic feedbacks between these systems remain debated.

Different atmospheric circulation pathways (or teleconnections) have been invoked to connect climate features across latitudes in past climate such as atmospheric pathways resulting from large interhemispheric thermal gradient (e.g., Chiang et al., 2014; Lee et al., 2011) or the well-studied atmospheric pathways associated with the El Niño–Southern Oscillation (ENSO) phenomenon (e.g., Campos and Rondanelli, 2023; Ortega et al., 2019). Yet, uncertainties prevail regarding the timing and nature of these large-scale atmospheric connections in the past. These arise from the lack of high resolution spatial and temporal reconstructions of the SWW belt required to shed light on its interaction with other well-studied climate systems located further north. Here, we aim to investigate the atmospheric pathways acting on the west coast of South America and, thus, the Southern Hemisphere (SH) since the LGM.

The west coast of South America is well-suited to reconstruct past atmospheric pathways as regional precipitation, temperature and winds are highly sensitive to the location of the ITCZ, the SPH and the SWW belt. At tropical latitudes, precipitation regimes are controlled by the trade winds and the ITCZ (Garreaud, 2009; Strub et al., 1998). At subtropical latitudes, arid conditions are associated with the SPH, a high-pressure cell west of the South American landmass caused by the subsidence of air masses of the Hadley cell (Garreaud, 2009; Held and Hou, 1980; Strub et al., 1998). At subtropical to polar latitudes, the SWWs govern precipitation regimes (Garreaud, 2009; Strub et al., 1998). The ascent of moisture-laden air masses from the westerlies' storm track along the Andes generates orographic precipitations in Central and Southern Chile (e.g., Barrett et al., 2009; Garreaud, 2009). Any changes in the position or structure of these climate features caused by changes in atmospheric pathways should thus be translated by hydroclimate changes in South America. Reconstructing hydrological regimes along the west coast of South America can thus shed light on the past connections between these large-scale atmospheric features.

The last 20 kyr were characterized by major climate changes in South America, such as the Glacial-Interglacial transition. While the large-scale evolution of the ITCZ (e.g., Arbuszewski et al., 2013; Schneider et al., 2014) and the SWW belt (e.g., Kaiser et al., 2024; Lamy et al., 2001, 2010; Moreno et al., 2018, 2021) have been addressed in several studies, the exact timing of the migration of the SWW belt and its latitudinal extent still lacks clarity. This results from contrasting climate conditions reconstructed across sites along Chile for the same time periods. For instance, increasingly drier conditions were inferred between 13.5 and 11.5 ka BP at the latitude of 30°S (Bernhardt et al., 2017; Kaiser et al., 2024), while wetter conditions marked this period at the latitude of 34°S (Valero-Garcés et al., 2005). Several records also supported drier conditions along Chile between ca. 11 and 7 ka BP (Jara and Moreno, 2014; Jenny et al., 2002a), while some high-altitude records indicated increases in relative moisture during the same time period (e.g., Fiers et al., 2019; de Porras et al., 2014). Here we thus focus on generating a high-resolution reconstruction of the past evolution of continental hydrological regimes along Chile to shed light on the past evolution of the SWW belt and the SPH. We then use our reconstruction, that aligns with most existing records, to explore the large-scale forcings on South American climate.

We reconstruct past continental hydrological regimes along Chile using the hydrogen isotope composition of leaf-wax n-alkanes (^{2}H/H, expressed as δ^2H_{wax} measured on the long-chain n-alkanes n-C_{29} and n-C_{31}) of sediment deposited at 33°S and 36°S offshore Chile (Fig. 1 and Fig. S1 reported in the Supplementary Material). These records were supplemented with the previously published δ^2H_{wax} record of site GeoB7139-2 from Kaiser et al. (2024) to widen the scope of this study.

δ^2H_{wax} values recorded in marine sediments are mainly determined by the δ^2H composition of past meteoric waters (Gaviria-Lugo et al., 2023a; Sachse et al., 2004, 2006, 2012; Sessions et al., 1999) and thus can be used to trace past hydrological regimes (e.g., Kaiser et al., 2024; Polissar et al., 2009; Rach et al., 2014; Schefuß et al., 2005). However, they can also be influenced by changes in plant evapotranspiration (Kahmen et al., 2013a, b) and plant type (e.g., Collins et al., 2013; Liu and Yang, 2008; Niedermeyer et al., 2016). These secondary controls can be investigated with the carbon isotope composition of leaf-wax long chain n-alkanes ($^{13}C/^{12}C$, expressed as $\delta^{13}C_{wax}$ measured on the long-chain n-alkanes n-C_{29} and n-C_{31}). To confirm the dominant role of past hydrology in altering δ^2H_{wax} values along Chile, we therefore measured $\delta^{13}C_{wax}$ values for the marine sites as well as for the modern fluvial sediments and marine surface sediments of Gaviria-Lugo et al. (2023a, b). Here, we show that the δ^2H_{wax} values from the last 20 kyr can be interpreted as archives of past precipitation δ^2H values, which we subsequently use to reconstruct past evolution of South American hydroclimate. Specifically, we reconstruct the past extent of SPH- and SWW-driven moisture and use this new reconstruction to investigate the atmospheric pathways acting on the South American climate since the LGM.

https://doi.org/10.5194/egusphere-2025-3153
Preprint. Discussion started: 10 July 2025

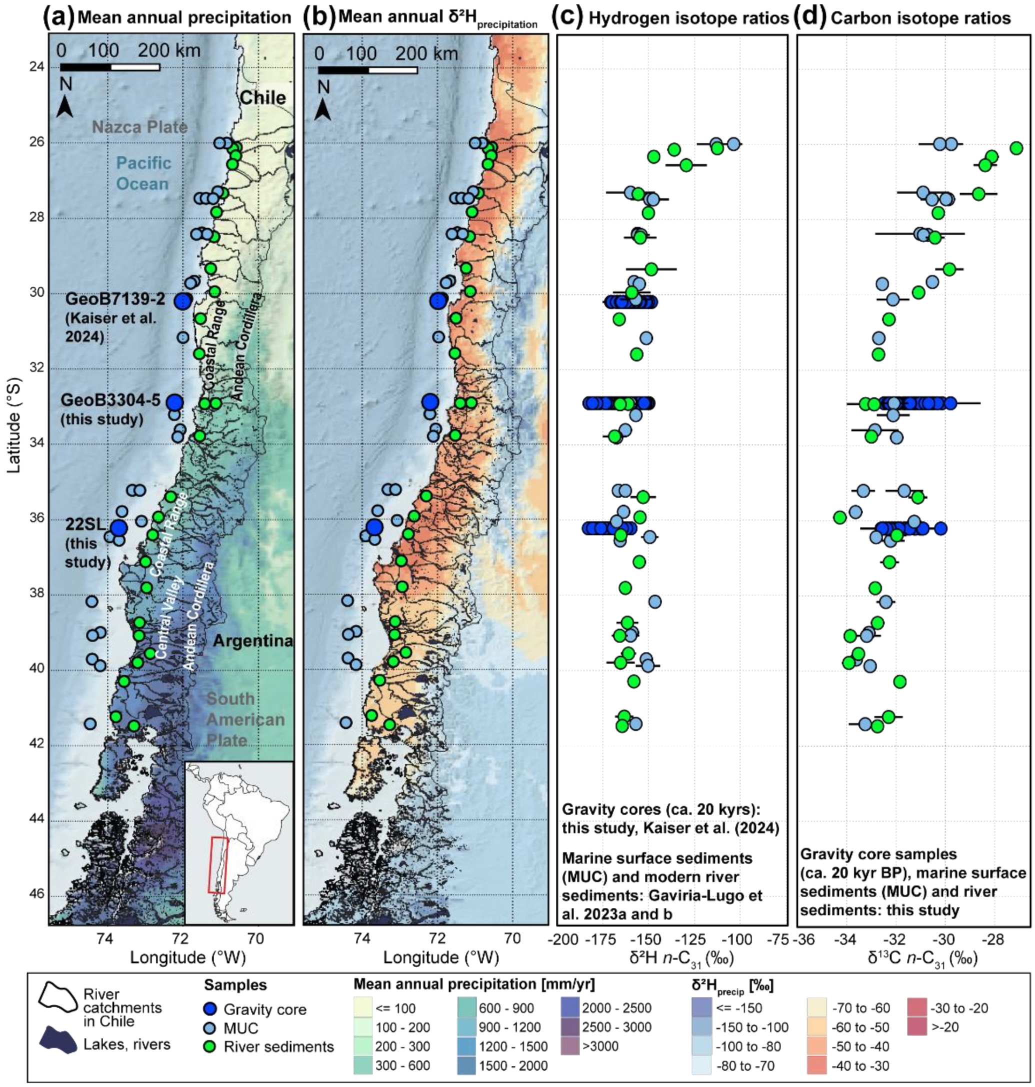

Figure 1. Sampling sites and the hydrogen and carbon isotope ratios (measured on *n*-C31 *n*-alkanes) of fluvial and marine sediments along Chile. Data represent present-day conditions (river and multicorer [MUC] sediments) and variability spanning ca. 20 kyr in gravity cores. (a) Mean annual precipitation map (TRMM 3B43, European Commission, Joint Research Centre (JRC), 2015) and sampling sites (this study, Gaviria-Lugo et al., 2023a; Kaiser et al., 2024). (b) Mean annual δ^2H_{precip} map (Bowen et al., 2005; Bowen and Revenaugh, 2003; Waterisotopes Database, 2017) and sampling sites (this study, Gaviria-Lugo et al., 2023a; Kaiser et al., 2024). (c) Hydrogen isotope composition (n-C_{31}) of modern fluvial sediments (green, Gaviria-Lugo et al., 2023a, b), marine surface sediments (MUC, light blue, Gaviria-Lugo et al., 2023a, b) and gravity cores (dark blue, site GeoB7139-2 from Kaiser et al., 2024 and sites GeoB3304-5 and 22SL) by latitude. (d) Carbon isotope composition (n-C_{31}) of fluvial sediments (green), marine surface sediments (light blue) and gravity cores (dark blue) by latitude (this study, see Gaviria-Lugo et al., 2023a for sample site description). The $\delta^{13}C$ ratio of modern river and MUC samples were corrected for the pre-industrial carbon isotope composition of the atmosphere (Sect. 3.4). Note the consistency of the modern hydrogen and carbon isotope ratios along Chile despite substantial changes in the mean annual precipitation amount (panel A). Digital Elevation Model is from the GEBCO Bathymetric Compilation Group (2019)(The GEBCO_2019 Grid - a continuous terrain model of the global oceans and land., 2023). The lake and river maps are from the Biblioteca del Congreso Nacional de Chile (accessed 31.03.2025). Watersheds are from Gaviria-Lugo et al. (2023a). Error bars in panels C and D correspond to two standard deviations (2σ) calculated from the δ^2H and the $\delta^{13}C$ values reported in Tables S5 to S7 (Läuchli et al., 2025, see Data availability) .

https://doi.org/10.5194/egusphere-2025-3153
Preprint. Discussion started: 10 July 2025

2 Study area

2.1 Geological setting and site selection

The Chilean active margin is ideal to study past continental environments as distances are relatively short between erosional zones (i.e., the Andean and the Coastal Cordillera) and the depositional zones on the Chilean continental margin (Fig. 1, Bernhardt et al., 2017). Between 30°S and 36°S, sediments are mainly transported to the Pacific Ocean by rivers. Aeolian transport of sediments – occurring today in the hyper-arid to arid regions of northern Chile – was likely minor south of 33°S during the last 20 kyr (Lamy et al., 1998; Stuut et al., 2007; Stuut and Lamy, 2004). We therefore consider the signal of modern fluvial sediments recorded by Gaviria-Lugo et al. (2023a, b) as representative of continental conditions and use it to calibrate the signal recorded in marine archives. The dataset reported is Gaviria-Lugo et al. (2023a, b) is composed of fluvial and marine surface sediments. The fluvial sediments were sampled in March 2019 near the mouth of the main rivers or streams along Chile (26°S - 42°S, Fig. 1), as well as in two smaller catchments in the Coastal Cordillera. The marine surface sediments (MUC) are from the R/V SONNE cruise-SO156 (Hebbeln and Shipboard Scientists, 2001) and the R/V SONNE cruise SO-102 (Hebbeln and Shipboard Scientists, 1995).

We selected two sediment gravity cores to reconstruct past hydrological changes (Fig. 1). At 33°S, core GeoB3304-5 (32.89°S-72.19°W, R/V Sonne Cruise SO102, Hebbeln and Shipboard Scientists, 1995) comprises sediments transported by the Maipo and the Aconcagua Rivers. At 36°S near the mouth of the Biobío and the Itata Rivers, we selected core 22SL (36.22°S - 73-68°W, Sonne Cruise SO161-5, Wiedicke-Hombach and Shipboard Scientific Party, 2002). To extend the latitudinal coverage of this study, we combined these two records with the published δ^2H_{wax} record of site GeoB7139-2 (30.20°S-71.98°W, R/V Sonne Cruise SO156, Hebbeln and Shipboard Scientists, 2001) from Kaiser et al. (2024). We also report new radiocarbon ages for these three sites. From a sedimentological point of view, site GeoB7139-2, located near the mouth of the Elqui and Limarí Rivers, closely resembles that of sites GeoB3304-5 and 22SL with source areas extending from the Pacific coast to the high Andes. The δ^2H_{wax} values measured at this site are thus considered directly comparable to the values reported for sites 22SL and GeoB3304-5. This contrasts with latitudes south of 41°S where source areas are restricted to lower altitudes due to important sediment storage associated with the Chilean Lake District (Bernhardt et al., 2017). Consequently, the δ^2H_{wax} record of site ODP1233 (41°S; Kaiser et al., 2024) is not directly compared to the records further north. This record is however addressed in the *Discussion*.

2.2 Climate features and temporal patterns along the west coast of South America

The ITCZ controls precipitation in northern South America (Fig. 2, e.g., Garreaud et al., 2009; Waliser and Gautier, 1993). The latitudinal position and the width of the ITCZ vary at different timescales (e.g., Haug et al., 2001b; Koutavas et al., 2006; Sachs et al., 2009; Yuan et al., 2023). The modern ITCZ migrates in the Pacific region between approximately 10°N in the austral winter to approximately 2-5°N during the austral summer, with a southern extent reaching northern Peru (Fig. 2a and b; Garreaud, 2009; Strub et al., 1998). These seasonal oscillations resemble the trends detected at longer timescales that suggest a migration of the ITCZ to the warmer hemisphere caused by cross-equatorial heat transport (e.g., Haug et al., 2001b; Koutavas et al., 2006; Schneider et al., 2014). This highlights a strong control of temperature differences between the hemispheres, and the energy balance in the tropics on the position of the ITCZ from decadal to orbital timescales (Mohtadi et al., 2016).

The position and intensity of the SPH controls the climate in central Chile (Fig. 2; Ancapichún and Garcés-Vargas, 2015; Barrett and Hameed, 2017; Dima and Wallace, 2003; Garreaud et al., 2009; Strub et al., 1998). At present, the southern extent of the SPH causes warm and dry conditions as far south as ca. 35°S during the austral summer (Fig. 2b), while its southern boundary shifts northward during the austral winter, following the migration of the polar front of the SWWs to around 27°S in modern climate (Fig. 2a; Ancapichún and Garcés-Vargas, 2015; Flores-Aqueveque et al., 2020; Garreaud, 2009; Strub et al., 1998). In addition, the equatorward winds of the SPH enhance upwelling offshore Chile (e.g., Rahn and Garreaud, 2014; Schneider et al., 2017). The ascent of cold subsurface waters causes a cooler and drier atmosphere aloft, and fog formation (e.g., Garreaud et al., 2001, 2008). Moisture spells associated with the SPH are thus primarily sourced from local water.

The SWW belt lies at extratropical and subpolar latitudes (Fig. 2) and undergoes seasonal shifts in configuration (Fig. 2; e.g., Garreaud, 2009; Garreaud et al., 2009; Nakamura and Shimpo, 2004; Strub et al., 1998). During austral winter, modern SWWs split into a subtropical jet at ca. 30°S–35°S and a subpolar jet at ca. 50°S–60°S. During the austral summer, the two jets converge into a mid-latitude jet located around 40°S (Bals-Elsholz et al., 2001; Gallego et al., 2005; Garreaud et al., 2009; Inatsu and Hoskins, 2004; Nakamura and Shimpo, 2004). This results in latitudinal migration of SWW-driven precipitation in Chile (Garreaud et al., 2009). During winter, the strengthening of the subtropical jet shifts SWW-driven precipitation northward, while during the austral summer, the alignment of the SWWs with the mid-latitude jet shifts the SWW-driven precipitation southward (Nakamura et al., 2004). On the windward side of the Andes, the SWW-driven precipitation – modulated by the relative strength of the subtropical and mid-latitude jets – is furthermore divided into two zones: a *core* zone corresponding to the primary westerlies storm tracks and a *peripheral* zone influenced by the northward propagation of the disturbances from the *core* zone. During the austral summer and autumn, the SWW *core* zone is centered around 50°S and the SWW-driven disturbances (i.e., *peripheral* zone) extend up to ca. 35°S, where they are blocked by the SPH (see above; Strub et al., 1998). During winter, strong precipitation forming the SWW *core* prevails south of 40°S, while the strengthening of the subtropical jet drives the SWW-driven precipitation of the *peripheral* zone northward up to the latitude of 27°S, which corresponds to the southern front of the SPH (Barrett and Hameed, 2017; Flores-Aqueveque et al., 2020; Strub et al., 1998). In contrast to the moisture spells associated with the SPH, the SWW-driven precipitation thus originates from more distant water sources along the storm track.

Climate phenomena acting at intra-annual to decadal timescales influence the west coast of South America. These include the El-Niño Southern Oscillation (ENSO; e.g., Cai et al., 2020; Garreaud et al., 2009; Montecinos and Aceituno, 2003), the Pacific (Inter)Decadal Oscillation (PDO or ENSO-like variability; e.g., Garreaud et al., 2009; Garreaud and Battisti, 1999; Zhang et al., 1997), the Southern annular mode (Gillett et al., 2006; SAM or Antarctic Oscillation; e.g., Gong and Wang, 1999; Marshall, 2003; Thompson and Wallace, 2000) and the Madden-Julian Oscillation (e.g., Madden and Julian, 1994). Most interannual variance in temperature and precipitation in South America can be explained by ENSO, the PDO and the SAM (Garreaud et al., 2009; Grimm, 2011; Thompson and Wallace, 2000). Here, as the PDO conditions resemble ENSO conditions (further termed here as ENSO-like conditions; Garreaud et al., 2009; Garreaud and Battisti, 1999), we focus on the SAM and the ENSO phenomena.

The SAM affects extra-tropical latitudes in the SH (Garreaud et al., 2009; Gillett et al., 2006; Thompson and Wallace, 2000) and refers to the latitudinal displacement of the SWW belt. A positive mode leads to a strengthened SWWs shifted poleward and a warming of the latitudes south of 40°S, while a negative SAM is associated with an equatorward shift of the SWWs (Garreaud et al., 2009; Thompson and Wallace, 2000). Whereas the SAM primarily affects the extra-tropical latitudes of the SH, the ENSO phenomenon influences all climate systems of South America (e.g., Cai et al., 2020; Garreaud et al., 2009).

The ENSO phenomenon consists of sea-surface temperature (SST) anomalies occurring irregularly every 2 to 7 years in the tropical Pacific (Diaz and Markgraf, 1992) with two typical modes, i.e., the classically defined El-Niño and La-Niña modes. During the positive or El-Niño (negative or La-Niña) phase of ENSO, warm (cold) SST anomalies are recorded in the tropical Pacific. During El Niño (La Niña) events, the ITCZ commonly migrates southward (northward) (e.g., Schneider et al., 2014) and has a wider (narrower) width (Fig. 2; Wodzicki and Rapp, 2020). These displacements are associated with changes in the atmosphere-ocean energy balance in the Tropics (Schneider et al., 2014). ENSO also tends to influence the central Pacific Hadley cells that contract equatorward (extended poleward) and strengthen (weaken) during El-Niño (La-Niña) modes (Li et al., 2023; Nguyen et al., 2013). This results in an equatorward shift of the contracted SPH during El Niño phases (Fig. 2d) and a southward extending SPH during La Niña phases (Fig. 2c; e.g., Campos and Rondanelli, 2023). Similar climate modulations have been observed in connection with the PDO (Ancapichún and Garcés-Vargas, 2015; Pezza et al., 2007). During El-Niño events, above-average precipitation also occurs in winter and spring across central Chile (ca. 27°S-35°S) reflecting a northward shift of SWW-driven precipitation caused by the contraction of the SPH and anticyclonic activities in the Amundsen-Bellingshausen Seas (Fig. 2d; Campos and Rondanelli, 2023; Montecinos and Aceituno, 2003). Conversely, below-average precipitation is associated with the La Niña phase, when the SPH moves south (Fig. 2c; Montecinos et al., 2000; Montecinos and Aceituno, 2003). Overall, the strong response of SWW-driven precipitation to SST anomalies near the Equator highlights the interconnectivity of SH climate features and underlines the presence of atmospheric pathways (or teleconnections).

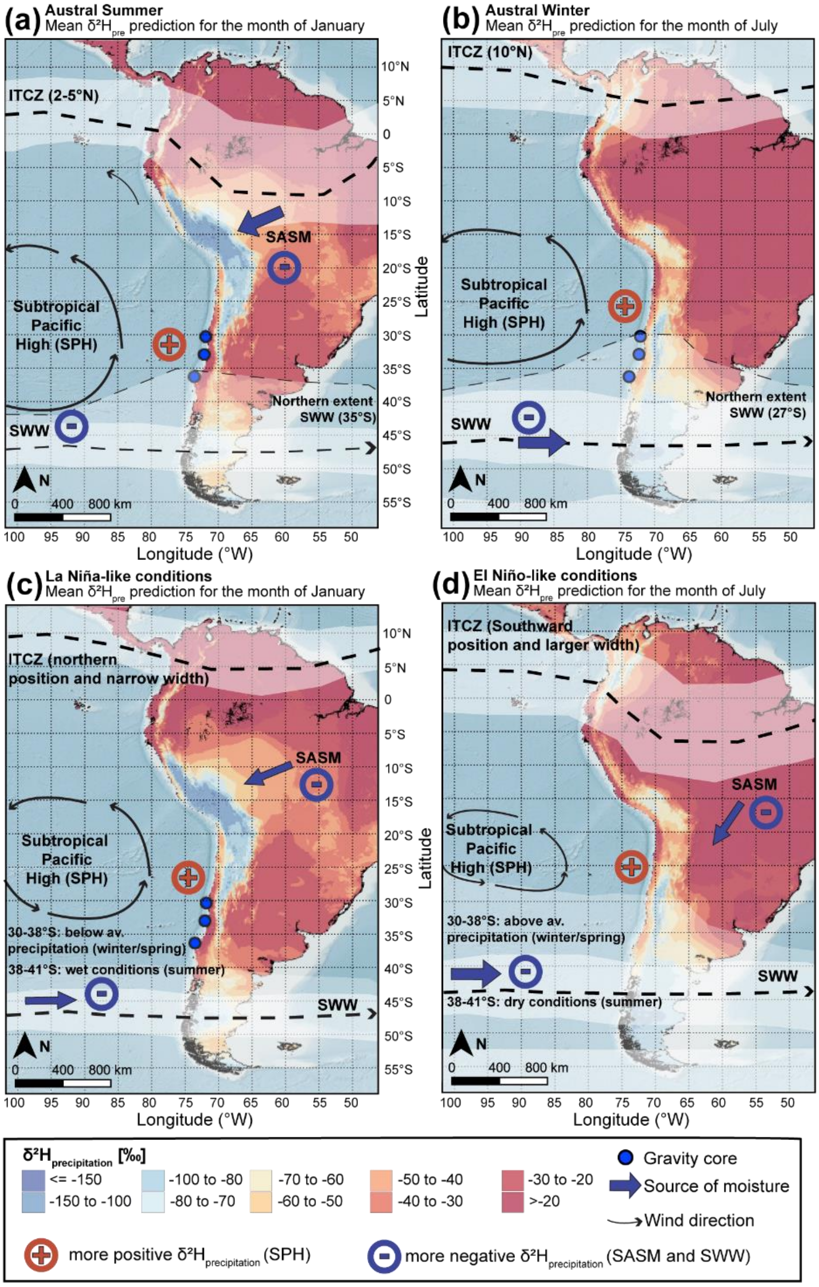

Figure 2. Schematic representation of the modern climate conditions on the west coast of South America. (a) Austral Summer, (b) Austral Winter, (c) La Niña-like conditions, (d) El Niño-like conditions. The blue arrows indicate the main source of moisture. The black arrows indicate wind direction and intensity. The dashed lines indicate the core of the ITCZ and the SWW belt. The blue minus and red plus signs indicate more negative and positive δ^2H_{precip} values, respectively. Note that these schematic climate conditions are described with a focus on the west coast of South America and are only broadly depicting the climate conditions of the Amazon basin and the east coast of South America (see SASM – South American Summer Monsoon). The blue dots correspond to the three marine sampling sites. Mean δ^2H_{precip} maps in January and July are from Bowen et al. (2005) and Bowen and Revenaugh (2003; Waterisotopes Database, 2017, accessed the 29.03.2024). The digital Elevation Model is from the GEBCO Bathymetric Compilation Group (2019). Sects. 2.2 and 2.3 for references.

3 Methods

3.1 Sampling Strategy

The sampling strategy for the modern data set composed of fluvial sediments and used to calibrate the marine archives – for which we report carbon isotope analyses – is described in Gaviria-Lugo et al. (2023a). For hydrogen and carbon isotope analyses, the marine cores GeoB3304-5 (Hebbeln and Shipboard Scientists, 1995) and 22SL (Wiedicke-Hombach and Shipboard Scientific Party, 2002), consisting of approximately 9 meters of marine sediments, were sampled with a resolution of ca. 500 years per sample. One to two centimeters of fine hemipelagic sediments were sampled for each depth, specifically targeting the intervals showing low signs of reworking and an absence of turbidite deposits. The samples were stored in pre-combusted glass vials stored in a cold room. To refine age-depth models and complement previously published radiocarbon ages, approximately 50 g of fine hemipelagic sediments were sampled at each targeted depth at sites GeoB3304-5, 22SL and GeoB7139-2.

3.2 Radiocarbon age-depth models

We generated new age-depth models for the three marine sites discussed here using previously published radiocarbon ages (Bernhardt et al., 2015; De Pol-Holz et al., 2010; Martínez Fontaine et al., 2019; Mohtadi and Hebbeln, 2004) supplemented by a set of new radiocarbon ages measured at the Poznań Radiocarbon Laboratory. In total, 6 new radiocarbon ages were acquired on monospecific samples of *Globigerina bulloides* for site GeoB7139-2, to complete the dataset of Mohtadi and Hebbeln (2004) previously acquired on mixed planktic assemblages. For site GeoB3304-5, the radiocarbon ages published in Bernhardt et al. (2015) were supplemented with 7 new radiocarbon ages from *G. bulloide*s. For site 22SL, the existing radiocarbon ages of De Pol-Holz (2010) and Martínez Fontaine et al. (2019) from monospecific samples of *G. bulloides*, mixed planktic foraminifera assemblages and mixed benthonic foraminifera assemblages were supplemented by 6 new radiocarbon ages acquired on mixed benthic assemblages (due to the low concentration in planktic foraminifera in the uppermost two meters of sediment). We preferred previously published ages acquired on planktic foraminifera samples over benthic foraminifera samples for core sections with a high density of radiocarbon age measurements.

The age-depth models were generated using the BACON v3.2.0 Bayesian age-depth model algorithm developed by Blauuw and Christen (2011). Abrupt changes in sediment accumulation rates as well as turbidites were integrated in the models. To consider the complex ventilation history of the water masses along Chile, two different scenarios were modelled for each site (Sect. 4.1). The parameters used for each BACON age-depth model are detailed in Figs. S2 to S7 reported in the Supplementary Material.

3.3 Lipid extraction and *n*-alkane abundances

The lipid extraction method of the modern river and marine surface sediments for which carbon isotope measurements are reported here can be found in Gaviria-Lugo et al. (2023a). For the marine hemipelagic sediments of sites GeoB3304-5 and

22SL, the samples were freeze-dried for 48 h and homogenized in an agate mortar before further treatment. Approximately 20 g of sediments were used to extract and purify lipids following the procedure described in Rach et al. (2020). The total lipid extracts (TLE) were first extracted with a Dionex Accelerated Solvent Extraction system (ASE 350, ThermoFisher Scientific) at 100°C and 103 bar pressure using a dichloromethane (DCM): methanol (MeOH) mixture (9:1, v/v). Two extraction cycles of 20 min (static time) were used. The TLE were collected in combusted glass vials and evaporated with nitrogen and spiked with 10 µg of 5α-androstane as internal standard. The organic lipids were then purified and separated into aliphatic, aromatic and alcohol/ fatty acid fractions by manual solid phase extraction (SPE) using 8 mL glass columns filled with 2 g of silica gel. Hexane, Hexane: DCM (1:1) and DCM: Methanol (1:1) were used to extract the different fractions. The aliphatic and aromatic fractions showing signs of sulfur were desulfurized by elution with active copper powder. All aliphatic fractions were cleaned by silver nitrate-coated silica gel to remove unsaturated compounds.

The *n*-alkanes contained in the aliphatic fraction were quantified with an Agilent 7890A gas chromatograph (GC) with a 30 m Agilent DB-5MS UI column (0.25 µm film thickness, 25 mm diameter). The GC was coupled to a flame ionization detector (FID) and an Agilent 5975C mass spectrometer (MS). The internal standard was used to normalize the peak areas of *n*-alkane and the results normalized to the initial dry weight used for the TLE.

The abundance of the *n*-alkanes was assessed by the total concentration of the odd-numbered-*n*-alkanes C_{25} to C_{33} of the dry weighted samples. Furthermore, the distribution of the *n*-alkanes was evaluated using the *n*-alkane average chain length (ACL) index (i.e., the weighted abundance of higher plant *n*-alkanes, C_{25}-C_{35}). The ACL index was calculated using the odd-carbon numbered *n*-alkanes C_{25} to C_{33} due to the low abundance of C_{35} in some samples (Eq. 1).

$$ACL = \frac{25\times C_{25}+27\times C_{27}+29\times C_{29}+31\times C_{31}+33\times C_{33}}{C_{25}+C_{27}+C_{29}+C_{31}+C_{33}} \quad (1)$$

3.4 Hydrogen and carbon isotope analyses

Stable hydrogen (δ^2H) and the carbon (δ^{13}C) isotope ratios of the *n*-alkanes in the aliphatic fraction of the sites GeoB3304-5 and 22SL were measured with a Trace GC 1310 (ThermoFisher Scientific) coupled to a Delta V plus Isotope Ratio Mass Spectrometer (IRMS) (ThermoFisher Scientific) following the procedure described in Rach et al. (2020). 30 m Agilent DB-5MS UI columns (0.25 µm film thickness, 25 mm diameter) were used in the GC. The program used for the GC oven was described in Rach et al. (2014). All measurements were replicated and the average δ^2H values was determined for each sample. The associated standard deviation and the number of replicates are reported for each sample.

Before and after each sequence an *n*-alkane standard mix A6 (n-C16 to n-C30) from A. Schimmelmann (Indiana University) with known hydrogen isotope values was measured and used to correct and transfer the measured δ^2H values to the Vienna Standard Mean Ocean Water (VSMOW) scale. The mean standard deviation of all (n) measured for the *n*-C_{29} alkane was 1.31 ‰ (n = 198) and 1.08‰ for the *n*-C_{31} alkane (n=199). For all peaks of the A6 standard mix (n=900), we calculated a mean standard deviation of 1.25‰. The H3+ factor was determine before each sequence and had a mean of 5.76 ± 0.45 (n=7) over the measuring period.

The carbon isotope ratios of the fluvial and marine surface sediments presented in Gaviria-Lugo et al. (2023a) were acquired following the same procedure. To compare the carbon isotope composition of sedimentary archives from the pre-industrial period with recent sediments, we corrected the δ^{13}C composition of the modern sediments for changes in the carbon isotope composition of the atmosphere caused by anthropogenic activities (Suess effect). Atmospheric CO_2 δ^{13}C was ca. -6.6 ‰ before the Industrial Revolution and around -8.4 in 2015 (Graven et al., 2017). Here, the river sediments sampled in 2019 are regarded as integrating organic matter produced over 5 to 10 years and a correction of 1.8‰ ($\delta^{13}C_{atm\ 2015}$- $\delta^{13}C_{atm\ 1850}$) was thus applied to their δ^{13}C values. The marine surface sediments sampled between 1 and 2 cm below seafloor (cmbsf) are regarded as integrating over ca. 100 years assuming a sediment accumulation rate of 20 cm/kyr. A correction of 0.4 ‰ ($\delta^{13}C_{atm\ 1950}$- $\delta^{13}C_{atm\ 1850}$) was thus applied to their δ^{13}C values.

3.5 Statistical methods

In their mathematical form, ratios represent exclusively real positive numbers. Yet, most multivariate statistics were developed for datasets ranging from negative infinity to positive infinity (i.e., real numbers). The isotope ratios reported here were therefore processed using the theory of compositional data analysis (Aitchison, 1982, 2005; Weltje, 2002; Weltje et al., 1996). The isotope ratios were transposed from their conventional notation (δ^2H in ‰) into simple ratios ($R_{sample}/R_{standard}$, where R=H^2/H), before being converted into real-valued numbers by log-ratio transformations. The log-ratio transformed data were used to derive simple moving averages (n=15, on the time-series resampled at a frequency of 100 yr). All values were transformed back to their native space for further visualizations. Moving averages were used to detect increasing and decreasing trends in the δ^2H_{wax} records.

3.6 GIS methods

To evaluate the controls on the δ^2H_{precip} signature of modern precipitation along Chile, we extracted catchment-averaged δ^2H_{precip} values for the month of January, July and for the entire year from the raster maps of Bowen et al. (2005) and Bowen and Revenaugh (2003; Waterisotopes Database, 2017; annual mean, January and July maps) using catchment outlines from the HydroBASINS product (Level 6, Lehner et al., 2006; Lehner and Grill, 2013, Fig. 3 and Fig. S8 reported in the Supplementary Material). Catchment-averaged mean annual temperature and precipitation amount were also extracted from WorldClim (WorldClim v. 2.1, 1970-2000, ca. 5 km spatial resolution; Fick and Hijmans, 2017) and the TRMM 3B43 products (European Commission, Joint Research Centre (JRC), 2015), respectively.

4 Results

4.1 Age-depth models

New age-depth models were established for cores GeoB7139-2 (30°S), GeoB3304-5 (33°S) and 22SL (36°S) using previously published and newly acquired radiocarbon ages (Table S1 in Läuchli et al., 2025, see Data availability). As past changes in the deep ocean stratification are complex along Chile (De Pol-Holz et al., 2010; Haddam et al., 2018; Siani et al., 2013) and water masses with different reservoir ages likely influenced the study area (Martínez Fontaine et al., 2019), we consider two scenarios. In the first scenario, we use reservoir ages from offshore Chile combined with the atmospheric SHCal20 calibration curve (Hogg et al., 2020), while in the second scenario, we directly use the Marine20 calibration curve (Heaton et al., 2020) with local corrections to the global ocean reservoir.

In the first scenario, the sites are considered influenced predominantly by Subantarctic Water (SAAW) following scenario 1 of Martínez Fontaine et al. (2019). This is supported by the modern occurrence of SAAW at 28°S (Silva et al., 2009) and evidence for a predominant influence of the SAAW at 31°S before ca. 15.5 ka BP (Martínez Fontaine et al., 2019). After around 15.5 ka BP, evidence suggests a mixing of the SAAW, the Equatorial Subsurface Water (ESSW) and the Antarctic Intermediate Water (AAIW) at the studied sites (Martínez Fontaine et al., 2019). However, we followed a conservative approach and attributed the reservoir ages of the SAAW to the entire time-span investigated here as the proportion of the different water masses occurring at each site remains unknown. Furthermore, better constraints exist for the reservoir ages of the SAAW compared to the ESSW near the studied sites. The reservoir ages of the SAAW were determined at 47°S (Haddam et al., 2018; Siani et al., 2013), while the reservoir ages of the ESSW were constrained further away at the equator (Umling and Thunell, 2017). A modification of the reservoir age of the ESSW is also anticipated during its transport south due to potential mixing with Antarctic Intermediate Water (AAIW). A comparison of the reservoir ages of the ESSW and the SAAW suggests a difference of less than ca. 400 years for most of the periods where reservoir ages are available for both water masses since 20 ka BP. An exception occurred at around 14.4 ka BP during which a difference of about 1,200 years, caused by the relatively small reservoir ages reconstructed at the equator (Umling and Thunell, 2017), was observed between the reservoir ages of the ESSW and the SAAW. In scenario 1, uncertainties of less than about 400 yr are therefore implied for the reservoir ages over the last 20 kyr, with potentially higher uncertainties between 13.8 and 14.8 ka BP. For the first scenario, we thus combined the reservoir ages characterizing the SAAW water mass, as published in Haddam et al. (2018) and Siani et al. (2013), with the SHCal20 calibration curve (Hogg et al., 2020) to reconstruct age-depth models.

In the second scenario, the Marine20 calibration curve (Heaton et al., 2020) was applied directly with corrections to the global ocean reservoir (ΔR) based on *n* reservoir age deviation from Merino-Campos et al. (2019) reported in the http://calib.org/marine/ database as follows: -55 ± 25 yr for site GeoB7139-2 (n=1), 19 ± 85 yr for site GeoB3304-5 (n=6, weighted mean) and 49 ± 30 yr for site 22SL (n=6, weighted mean).

In both scenarios, the radiocarbon ages obtained from benthic foraminifera, under the influence of deeper water masses, were corrected using the offsets between benthic and planktic radiocarbon ages reported by Siani et al. (2013) at site MD07-3088 (46°S, 1,536 m water depth).The reservoir ages and offsets used in each scenario are provided in Table S1 (Läuchli et al., 2025, see Data availability).

The modelled sediment ages span 36 and 1 ka BP (Scenarios 1 and 2, Table S2 in Läuchli et al., 2025, see Data availability) for site GeoB7139-2, and up to about 24 ka BP and 20 ka BP for sites GeoB3304-5 and 22SL, respectively (Scenarios 1 and 2, Tables S3 and S4 in Läuchli et al., 2025, see Data availability). The differences between the two scenarios modelled are reported in the Tables S2 to S4 (Läuchli et al., 2025, see Data availability). Reconstructions based on scenario 2 generally yielded older ages compared to those of scenario 1. For sites GeoB7139-2 and GeoB3304-5, the largest differences inferred for the two scenarios during the last 25 kyr were approximately 900 years (Tables S2 and S3 in Läuchli et al., 2025, see Data availability). In contrast, differences up to 2,400 years were recorded in site 22SL (between ca. 7 and 9 ka BP in scenario 1). These discrepancies highlight the relatively large uncertainties associated with the age models developed here and the ages inferred throughout this work. However, we consider scenario 1 to more accurately reflect the complex stratification and mixing of the water masses of the study area, which may not be fully captured by the Marine20 calibration curve based on a global-scale simulation. Therefore, we used scenario 1 for further analyses in this study.

4.2 Biomarker analyses

4.2.1 Average chain lengths (ACL) and abundances of *n*-alkanes

The abundance and distribution of *n*-alkanes in samples from sites GeoB3304-5 and 22SL are reported in Tables S5 and S6 (Läuchli et al., 2025, see Data availability). At site GeoB3304-5 (33°S), *n*-alkane concentrations varied between 0.24 and 4.75 $\mu g\ g^{-1}$ sediment dry weight (dw). At site 22SL (36°S), the *n*-alkane concentrations ranged between 0.42 and 3.4 $\mu g\ g^{-1}$ dw. Similar ACL were derived for both sites with values ranging between 29.2 and 30 for site GeoB3304-5 and 29.5 and 30 for site 22SL (Tables S6 and S7 in Läuchli et al., 2025, see Data availability). The two most abundant odd-numbered *n*-alkanes were *n*-C_{29} and *n*-C_{31}, with slightly higher concentrations for the *n*-C_{31} homologue. No clear trend was detected in the abundance and distribution of the *n*-alkanes in the marine archives.

4.2.2 Leaf-wax *n*-alkane hydrogen isotope ratios of the marine sites

The hydrogen isotope compositions (δ^2H_{wax}, *n*-C_{31}) of sites GeoB3304-5 and 22SL varied between -188 and -154 ‰ and -188 and -164 ‰, respectively (Figs. 4 and 5, Tables S5 and S6 in Läuchli et al., 2025, see Data availability), while the δ^2H_{wax} values of the *n*-C_{29} records varied between -181 and -145 ‰ and -181 and -155 ‰, respectively (Figures S11 and S13 reported in the Supplementary Material, and Tables S5 and S6 reported in Läuchli et al., 2025, see Data availability). The figures showing the *n*-C_{29} alkane records – closely resembling the δ^2H_{wax} *n*-C_{31} values albeit with overall higher δ^2H_{wax} – are included in the *Supplementary Material* (Figs. S9 to S13 reported in the Supplementary Material) as not allowing a direct comparison with the δ^2H_{wax} *n*-C_{31} record of Kaiser et al. (2024). In site 22SL, δ^2H_{wax} values smoothed using a 1500-year moving average (Sect. 3.5) are relatively stable over time, despite relatively high dispersions of the data (Fig. 4 and Fig. S11 reported in the Supplementary Material) and an increase detected in the δ^2H_{wax} *n*-C_{31} values between 15 and 13 ka BP (Fig. 4 and Figs. S10 and S11 reported in the Supplementary Material). At site GeoB3304-5, similar fluctuations were detected in the moving average-smoothed δ^2H_{wax} records of the *n*-C_{29} and *n*-C_{31} alkanes (Fig. S9 reported in the Supplementary Material). These data suggest past changes in the δ^2H_{precip} signals along Chile.

4.2.3 Carbon isotope ratios ($\delta^{13}C_{wax}$) of fluvial and marine sediments

The carbon isotope ratios ($\delta^{13}C_{wax}$) of leaf-wax *n*-alkanes in fluvial sediments, corrected for the pre-industrial carbon isotope composition of the atmosphere, ranged from -34.6 to -26.8‰ (*n*-C_{31}) and -34.2 to -27.1 ‰ (*n*-C_{29}, Fig. 1d, Table S7 in Läuchli et al., 2025, see Data availability). The $\delta^{13}C_{wax}$ of marine surface sediments, corrected for the pre-industrial carbon isotope composition of the atmosphere, ranged from -34 to -29.9‰ (*n*-C_{31}) and -33.6 to -29.3‰ (*n*-C_{29}, Fig. 1d, Table S7 in Läuchli et al., 2025, see Data availability). At site GeoB3304-5, the $\delta^{13}C_{wax}$ values varied between -32.7 and -29.9‰ for the *n*-C_{31} *n*-alkane homologue and -32.6 and -29.3‰ for the *n*-C_{29} *n*-alkane homologue (Fig. 4 and Fig. S11 reported in Supplementary Material, Table S5 reported in Läuchli et al., 2025, see Data availability). For site 22SL, the carbon isotope ratios ranged between -32.8 and -29.9‰ for the *n*-C_{31} *n*-alkane homologue and -32.9 and -30.4‰ for the *n*-C_{29} *n*-alkane homologue homologue (Fig. 4, Fig. S11 reported in Supplementary Material, Table S4 reported in Läuchli et al., 2025, see Data availability). Relatively stable moving averages were detected in the carbon isotope records at sites GeoB3304-5 and 22SL with both sites displaying similar ranges of values (Fig. 4 and Fig. S11 reported in Supplementary Material).

4.2.4 Catchment-averaged climate variables and δ^2H values of modern precipitations along Chile

Catchment-averaged δ^2H_{precip} values are shown in Fig. 3 and reported in Table S8 (Läuchli et al., 2025, see Data availability). The modern mean annual catchment-averaged δ^2H_{precip} values ranged between ca. -103 and -44‰. Modern mean catchment-averaged δ^2H_{precip} values ranged between -104 and -23 ‰ for January and between -105 and -28‰ for July. The modern mean catchment-averaged temperature and precipitation amounts are reported in Table S8 (Läuchli et al., 2025, see Data availability).

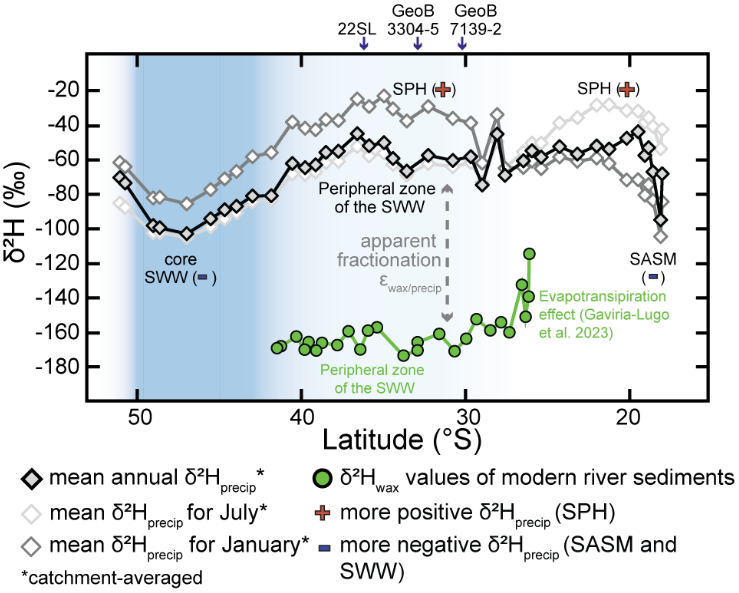

Figure 3. Modern catchment-averaged δ^2H_{precip} values and δ^2H_{wax} values from major river sediments (Gaviria-Lugo et al., 2023a, b) by latitude in Chile. Note the negative signal of the SWW belt in the three δ^2H_{precip} models reported here. During austral summer (January), the SPH, characterized by higher δ^2H_{precip} values due to the more local origin of vapor, is recorded as far south as ca 35°S (Sect. 2.2). The more negative δ^2H_{precip} values detected north of 27°S are associated with the South American Summer Monsoon and thus vapor source from the amazonian basin. During austral winter, the peripheral zone of the SWWs influences precipitation as far north as 27°S, north of which δ^2H_{precip} values reflect the SPH. Mean annual δ^2H_{precip} values are mainly controlled by SWW-driven precipitation south of 27°S, as these values resemble those of July, and the SASM-driven precipitation north of 27°S, as values then resemble those of January. The δ^2H_{wax} values of modern river sediments integrating annual precipitation (Gaviria-Lugo et al., 2023a, b) reflect the signal of the peripheral zone of the SWWs. The blue gradient is a schematic representation of the SWW core and peripheral zones.

5. Discussion

5.1 $\delta^{13}C_{wax}$ values as recorders of past changes in plant water use efficiency along Chile

The carbon isotope ratios of leaf-wax *n*-alkanes (expressed as $\delta^{13}C_{wax}$ values) are mainly controlled by plant ecophysiology (i.e., C_3 or C_4 pathway plant assemblages) and their response to water availability (i.e., water-use efficiency; e.g., Bi et al., 2005; Diefendorf et al., 2015; Liu et al., 2015). At present, the latitudes between 26°S and 41°S are characterized by highly heterogenous vegetation, mostly C_3 pathway plants (Powell and Still, 2009), and a strong climate gradient, yet the $\delta^{13}C_{wax}$ values from modern river sediments cluster between -34.6 and -31.3‰ (*n*-C_{31}) between 30°S and 42°S (Fig. 1d). This low variability in modern $\delta^{13}C_{wax}$ values is consistent with the predominance of C_3 pathway plants and/or suggests similar water use efficiency of the different plant assemblages between 30°S and 42°S despite the strong climate gradient of Chile.

The average $\delta^{13}C_{wax}$ values of sites GeoB3304-5 and 22SL remained relatively stable during the last 20 kyr (Fig. 4 and Fig. S11 reported in the Supplementary Material), despite evidence for vegetation changes (e.g., Heusser et al., 2006b; Werner et al., 2018). This suggests similar plant ecophysiology and/or water-use efficiency since the LGM and confirms the secondary role of vegetation type and ecophysiology in setting the isotope composition of leaf-wax plants *n*-alkanes along Chile.

At present, higher $\delta^{13}C_{wax}$ values characterize the modern arid and hyperarid conditions north of 30°S. The slightly higher $\delta^{13}C_{wax}$ values of the marine archives compared to the present values (corrected for pre-industrial $\delta^{13}C$ levels, Fig. 1d) thus suggest overall drier conditions than present at latitudes of 33°S and 36°S over the last 20 kyr. Nevertheless, $\delta^{13}C_{wax}$ values above -28 ‰ are absent in the paleorecords. Such values are characteristic of modern latitudes north of 27°S (Fig. 1) and are attributed to plant and soil water evapotranspiration under hyperarid conditions that also affect the hydrogen isotope ratios (Gaviria-Lugo et al., 2023a). We thus hypothesize that the hyperarid conditions of today north of 27°S never occurred at 33°S and 36°S during the last 20 kyr.

5.2 Leaf-wax *n*-alkane hydrogen isotope ratios as a moisture source proxy along Chile

The $\delta^{2}H$ values of leaf-wax *n*-alkanes (Fig. 4 and Fig. S11 reported in the Supplementary Material) are mainly controlled by the isotope signature of local meteoric waters ($\delta^{2}H_{precip}$) (Gaviria-Lugo et al., 2023a; Sachse et al., 2012). Gaviria-Lugo et al. (2023a) assessed the factors controlling $\delta^{2}H_{wax}$ along Chile and found that modern continental meteoric water $\delta^{2}H$ is robustly recorded in offshore $\delta^{2}H_{wax}$ records under humid to arid conditions, while vegetation type is not a significant parameter. With the onset of hyperaridity the relationship between meteoric water $\delta^{2}H$ and $\delta^{2}H_{wax}$ ceases to be linear and plant and soil water evapotranspiration additionally leads to higher $\delta^{2}H_{wax}$ signal (>ca. -150 ‰) – confirming sedimentary $\delta^{2}H_{wax}$ as a robust recorder of hydrological change. As high $\delta^{2}H_{wax}$ values (>ca. -150 ‰) do not occur in the marine archives, we interpret the past $\delta^{2}H_{wax}$ records as past changes in $\delta^{2}H_{precip}$ composition.

The main controls on $\delta^{2}H_{precip}$ values are air temperature (itself controlled by latitude and elevation, Bowen et al., 2019; Dansgaard, 1964; Rozanski et al., 1993), rainfall amount in tropical regions (Bowen et al., 2019; Dansgaard, 1964), continental re-evaporation (Bowen et al., 2019; Salati et al., 1979) and/or the moisture source region and vapor transport (Bailey et al., 2018; Bowen et al., 2019; Putman et al., 2017; Tian et al., 2007). The short and homogenous distances to coastline along Chile suggest re-evaporation is unlikely to affect $\delta^{2}H_{precip}$ values (i.e., $\delta^{2}H_{wax}$ values along Chile). Low to absent correlations determined between catchment-averaged $\delta^{2}H_{precip}$ values and mean annual precipitation amount (r^2=0.22, n=39) also indicate negligible control on $\delta^{2}H_{precip}$ values by precipitation amount. Catchment-averaged $\delta^{2}H_{precip}$ values and mean annual temperature are correlated (r^2= 0.67, n=40 with an increase of ca. 6‰ per °C), although this partly results from the modelling of $\delta^{2}H_{precip}$ values as a function of altitude and latitude (i.e., temperature; Bowen et al., 2005; Bowen and Revenaugh, 2003). A direct comparison of modern $\delta^{2}H_{wax}$ values (*n*-C$_{31}$) and mean annual temperature from Gaviria-Lugo et al. (2023a) yields less correlation (r^2=0.4, n=26) suggesting a secondary role of temperature in setting $\delta^{2}H_{wax}$ ratios. This secondary role of temperature is confirmed by the divergent response of past $\delta^{2}H_{wax}$ records (sites GeoB3304-5 and 22SL) to similar changes in sea surface temperature (ca. 4°C between 17 and 11 ka BP) at 30°S (SST, UK'37 Index, site GeoB7139-2, Kaiser et al., 2008, 2024) and 36°S (SST, UK'37 Index, site ODP202-1234, de Bar et al., 2018a, Fig. 5). By a process of elimination, we thus consider $\delta^{2}H_{wax}$ ratios mostly controlled by moisture source origin and vapor transport.

https://doi.org/10.5194/egusphere-2025-3153
Preprint. Discussion started: 10 July 2025

We recognize four distinct δ^2H_{precip} signals along Chile based on the modern catchment-averaged δ^2H_{precip} values (Figs. 2 and 3). North of 27°S, catchment-averaged δ^2H_{precip} values more negative than ca. -60‰ (January) are associated with South American Summer Monsoon-driven precipitation (SASM, Figs. 2 and 3, e.g., Garreaud et al., 2009; Vera et al., 2006). Such δ^2H_{precip} values are consistent with water vapor transport over the Amazonian basin (Fig. 2). Note that north of 27°S, mean annual δ^2H_{precip} values are mainly governed by SASM-driven precipitation. Higher δ^2H_{precip} values (> -40‰, Figs. 2 and 3) between ca. 27°S and 35°S in January, and north of 27°S in July are consistent with SPH-associated moisture and its more local vapor sources (Sect. 2.2). Further south, SWW-driven precipitation controls δ^2H_{precip} values. Between ca. 45°S and 50°S, values as negative as -100‰ characterize the SWW *core*, while, further north, values around -60‰ characterize the *peripheral* zone of the SWW belt. Note that SWW-driven precipitation controls mean annual δ^2H_{precip} signals south of 27°S as these values resemble those of July (Fig. 3). Past changes in δ^2H_{precip} values (and thus δ^2H_{wax} values) at a fixed latitude thus reflect latitudinal migration of these climate features. As SASM-driven precipitation are largely limited to north of 27°S on the windward side of the Andes by the topographic barrier associated with the Arid Diagonal Zone (Luebert, 2021), we interpret past δ^2H_{wax} records between 30°S and 36°S in terms of precipitation associated with the SPH, the *peripheral* zone of the SWW belt and the SWW *core*.

We use the modern δ^2H_{wax} values of river sediments reported in Gaviria-Lugo et al. (2023a) to constrain the signal of the *peripheral* zone of the SWW belt. Under the assumption that modern river sediment δ^2H_{wax} ratios integrate precipitation over the entire year, the values reported in Gaviria-Lugo et al. (2023a) between 30°S and 42°S reflect the signal of the *peripheral* zone of the SWW belt (Fig. 3). We thus derived the 5th and 95th percentiles of the modern δ^2H_{wax} values of rivers located between 30°S and 42°S to classify past δ^2H_{wax} records. The δ^2H_{wax} values ranging between -178 ‰ and -156 ‰ (n-C_{29}) and -172 ‰ and -158 ‰ (n-C_{31}) were classified as under the influence of the *peripheral* zone of the SWW belt. Values above these ranges were classified as under the influence of the SPH and below, as indicating a closer proximity to the SWW *core* (Fig. 4 and Fig. S11 reported in the Supplementary Material). Note that, while the modern δ^2H_{precip} values cover a range of ca. 60‰, a maximum range of ca. 35‰ was recorded by the past δ^2H_{wax} values. This suggests that the latitude between 36°S and 30°S did not experienced the entire range of modern conditions (i.e., SWW *core* to SPH). Nevertheless, we interpret higher δ^2H_{wax} values as indicating a stronger influence of the SPH – that is, drier conditions –, while lower δ^2H_{wax} values reflect a stronger influence of the SWW *core* – meaning more frequent and intense precipitation.

5.3 Past hydrological regime in central Chile (30°S to 36°S)

Here, we first describe the origin of precipitation reconstructed at sites 22SL, GeoB3304-5 (this study) and GeoB7139-2 (Kaiser et al., 2024) and compare it with previously published paleoclimate reconstructions (Sects. 5.3.1 to 5.3.5).

Site 22SL (36°S) is characterized by δ^2H_{wax} values ranging between -181 and -155 ‰ (n-C_{29}) and -188 and -164 ‰ (n-C_{31}) that corresponds to an influence of the SWW belt (*peripheral* and *core* zones, Sect. 5.2). These δ^2H_{wax} records exhibit considerable scatter, which we attribute to the larger source area at this site compared to sites further north. The source area of site 22SL encompasses the catchments of the Itata and the Biobío Rivers between 36°S and 39°S, while narrower source areas centered around 33°S and 30°S characterize sites GeoB3304-5 and GeoB7139-2, respectively. The source area of site GeoB3304-5 corresponds to the catchments of the Maipo and the Aconcagua Rivers (34°S to 32°S) and the source area of site GeoB7139-2 to the catchments of the Elqui and Limarí Rivers (29°S to 31°S). The records at 36°S are thus more likely to integrate signals from two distinct climate features simultaneously and/or a larger portion of the latitudinal δ^2H_{precip} range. Alternatively, some alteration of δ^2H_{wax} signals before deposition by mixing with the older sediments stored in the Central Valley (Fig. 1; Lowrie and Hey, 1981) could also explain the dispersion of the data at 22SL, yet the clear trends detected in the nearby high-resolution pollen records of site ODP1234 (<1 km, Heusser et al., 2006a) suggest terrestrial signals were not significantly altered before deposition. Despite this large scatter, a trend was detected in the δ^2H_{wax} n-C_{31} record at 36°S, with lower δ^2H_{wax} values before 14.5 ka BP, suggesting a stronger influence of the SWW *core*, and slightly higher δ^2H_{wax} *n*-C_{31} values after 14.5 ka BP suggesting an influence of the *peripheral* zone of the SWW belt (Fig. 4). The relatively stable δ^2H_{wax} *n*-C_{29} values additionally suggest a persistent influence of the *peripheral* zone of the SWW belt over the last 20 kyr (Fig. S11 reported in the Supplementary Material). We thus infer a continuous influence of SWW-driven precipitation in the source area of site 22SL for the studied time-span with a potential stronger influence of the SWW *core* before ca. 14.5 ka BP.

At 33°S (site GeoB3304-5), δ^2H_{wax} values suggest an influence of both the SPH and the SWW belt on local meteoric water composition over the last 20 kyr. Before 17 ka BP, relatively low δ^2H_{wax} values indicate an influence of SWW *core* precipitation that aligns with the values detected further south (see site 22SL). It also agrees with the δ^2H_{wax} ratios (*n*-C_{31}) of site GeoB7139-2 (30°S; Kaiser et al., 2024) indicating an influence the *peripheral* zone of the SWW belt. We thus infer a northern extent of the SWW belt during the LGM (Fig. 4 and Fig. S11 reported in the Supplementary Material). The following increases in δ^2H_{wax} values detected at sites GeoB3304-5 (this study) and GeoB7139-2 (Fig. 4, Kaiser et al., 2024) between ca. 17 and 14 ka BP (this study) and ca. 17 and 13 ka BP, respectively, then suggest a southward migration of the SWW belt. This southward migration was likely interrupted between 14 and 11.5 ka BP as a slight decrease in the δ^2H_{wax} value is recorded at 33°S (Fig. 4). Despite these fluctuations, the δ^2H_{wax} records indicate a dominant influence of the SWW belt at 33°S until ca. 11.5 ka BP. Between 11.5 and 7 ka BP, an influence of both the SPH and the SWW belt is detected at 33°S, with δ^2H_{wax} values ranging between those of sites GeoB7139-2 (30°S, Kaiser et al., 2024) and 22SL (36°S). Site GeoB3304-5 thus likely lay at the boundary between the SPH and the SWW belt at that period, which implies a southward and contracted SWW belt. Between 7 and 5.5 ka BP, a clear influence of SPH-associated moisture is then recorded at 33°S (Fig. 4 and Fig. S11 reported in the Supplementary Material) confirming the southward position of the SWW belt. During the last 5.5 kyr, the δ^2H_{wax} records from sites GeoB7139-2 and GeoB3304-5 then converge toward the values recorded further south. This suggests a gradual return northward of SWW-driven precipitation that aligns with the relatively homogenous δ^2H_{wax} values recorded at present along Chile (Figs. 1 and 3, Gaviria-Lugo et al., 2023a). Note that at around 4 ka BP, high variability characterizes the δ^2H_{wax} *n*-C_{29} values of site GeoB3304-5 (Fig. S11 reported in the Supplementary Material), which potentially indicates abrupt climate changes. Overall, the δ^2H_{wax} records of site GeoB3304-5 highlight the strong sensitivity of the latitude of 33°S to past displacements of the SWW belt and the SPH.

The reconstruction of the latitudinal displacement of SSW- and SPH-driven precipitation at 33°S and 30°S allows defining five time periods, or phases. Phase I (25-17 ka BP) is characterized by an influence of the SWW *core* extending northward to about 33°S. During Phase II (17-14 ka BP), a progressive increase in the δ^2H_{wax} values suggests a southward migration of SWW-driven precipitation. Phase III (14-11.5 ka BP) is defined by a pause in the southward migration of the SWW belt detected at 33°S. The SPH and the SWW belt likely reached their southernmost position during Phase IV (11.5-5.5 ka BP). The Phase IV is subsequently separated in Phase IV A and B as climate changes were detected south of 36°S during this period (Sect. 5.3.4). Phase V (last 5.5 kyr) is marked by a return northward of the influence of the *peripheral* zone of the SWW belt up to at least the latitude of 30°S and higher climate variability. Note that relatively high uncertainties are associated with timings of transitions between phases reflecting the uncertainties on the age-depth models (Sect. 4.1). We also acknowledge time lags effects between the different records discussed throughout this work, which we attribute to different age model calibrations (e.g., Lamy et al., 1999), low age model resolutions (e.g., Valero-Garcés et al., 2005), different response times of the proxies used (e.g., Tofelde et al., 2021). The ages determined in this study are thus regarded as broad estimates.

To validate our results, we compare them with previously published climate reconstructions extending as far south as 56°S to capture the entire structure of the SWW belt. The relative changes in the hydrological regimes of each record are summarized in Fig. 4 and Figs. S11 and S12 reported in the Supplementary Material. Note that we consider here almost exclusively past reconstruction of hydrological regimes from low-altitude sites on the windward side of the Andes, as high-altitude or leeward records were potentially influenced by the climate of the lee side of the Andes (e.g., Quade and Kaplan, 2017; Tiner et al., 2018). The overall agreement between past climate conditions inferred from previously published reconstructions and those inferred from past δ^2H_{wax} values corroborate the use of the modern δ^2H_{wax} ratios to calibrate past δ^2H_{wax} records.

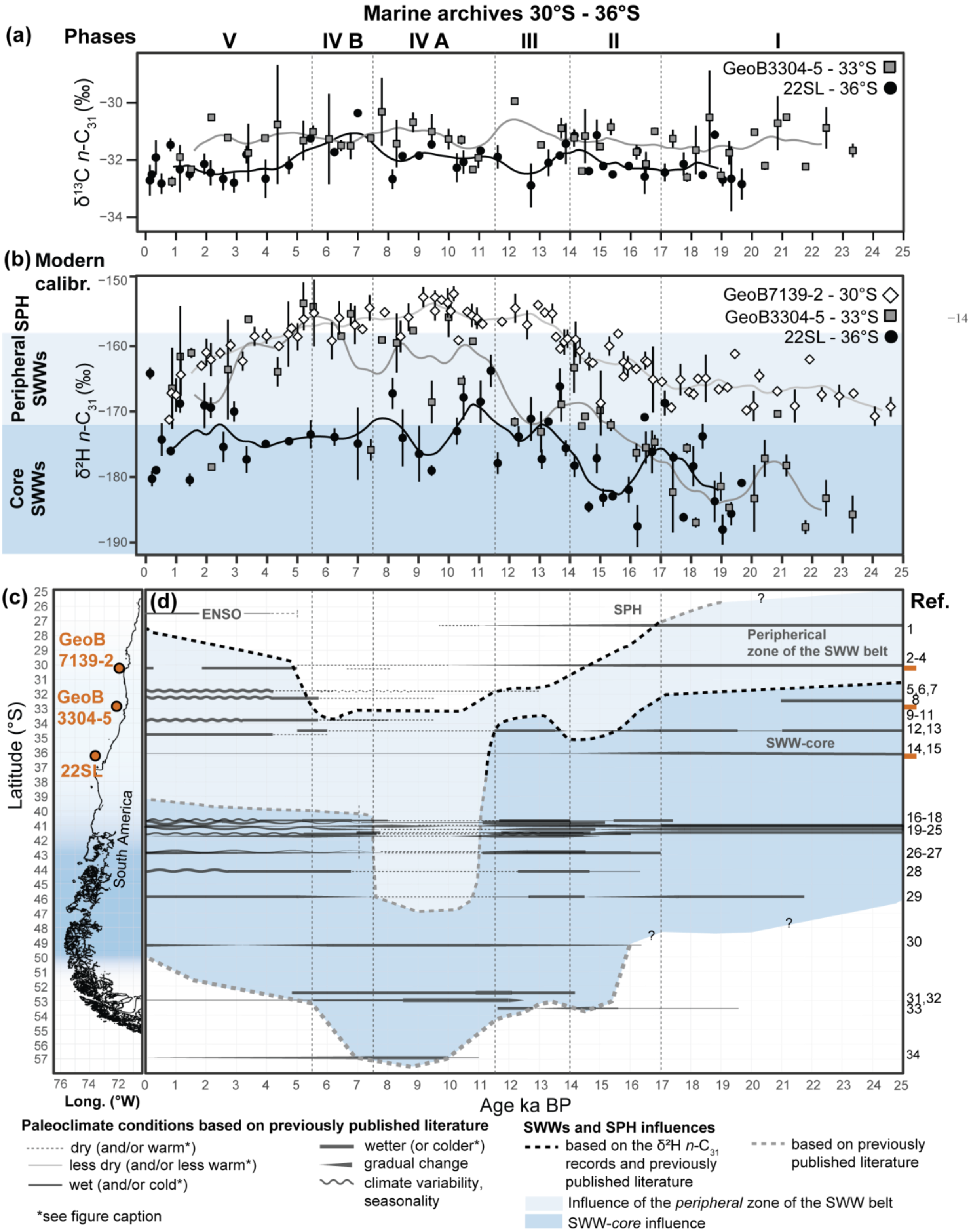
Marine archives 30°S - 36°S
(a) Phases
V
IV B
IV A
III
II
I
δ13C n-C31 (‰)
GeoB3304-5 - 33°S
22SL - 36°S
(b) Modern calibr.
SPH
Peripheral SWWs
Core SWWs
δ2H n-C31 (‰)
GeoB7139-2 - 30°S
GeoB3304-5 - 33°S
22SL - 36°S
−14
(c)
GeoB 7139-2
GeoB 3304-5
22SL
Latitude (°S)
South America
Long. (°W)
(d)
ENSO
SPH
Peripherical zone of the SWW belt
SWW-core
?
Ref.
1
2-4
5,6,7
8
9-11
12,13
14,15
16-18
19-25
26-27
28
29
30
31,32
33
34
Age ka BP
Paleoclimate conditions based on previously published literature
dry (and/or warm*)
less dry (and/or less warm*)
wet (and/or cold*)
wetter (or colder*)
gradual change
climate variability, seasonality
*see figure caption
SWWs and SPH influences
based on the δ²H n-C31 records and previously published literature
based on previously published literature
Influence of the peripheral zone of the SWW belt
SWW-core influence

Figure 4 Reconstruction of the past extent of the SWW belt and the SPH based on the hydrogen isotope records of leaf-wax *n*-alkanes (*n*-C_{31}) and previously published literature. (a) δ^2H_{wax} records of sites GeoB7139-2 (30°S, Kaiser et al., 2024), GeoB3304-5 and 22SL (this study). (b) $\delta^{13}C_{wax}$ records of sites GeoB3304-5 and 22SL. (c) Map of the west coast of South America between the latitudes of 25°S and 56°S with the locations of the marine sites. (d) Reconstruction of the past extent of the SWW belt and the SPH. Note the southward migration of the SWW belt at around 17 ka BP, its northward migration during Phase III, its abrupt shift southward during Phase IV and its return northward during Phase V. References: (1) (Stuut and Lamy, 2004), (2) (Muñoz et al., 2020), (3) (Kaiser et al., 2008), (4) (Bernhardt et al., 2017), (5) (Ortega et al., 2012), (6) (Maldonado and Villagrán, 2002), (7) (Maldonado and Villagrán, 2006), (8) (Flores-Aqueveque et al., 2021), (9) (Jenny et al., 2002a), (10) (Jenny et al., 2003), (11) (Villa-Martínez et al., 2003), (12) (Valero-Garcés et al., 2005), (13) (Frugone-Álvarez et al., 2017), (14) (Heusser et al., 2006a), (15) (Muratli et al., 2010), (16) (Vargas-Ramirez et al., 2008)in which only a cooling was recorded during the ACR, (17) (Jara and Moreno, 2014), (18) (Jara and Moreno, 2012), (19) (Heusser et al., 2006b), (20) (Kaiser et al., 2024), (21) (Moreno et al., 2018), (22) (Moreno and León, 2003), in which only a cooling was recorded during the ACR (23) (Moreno and Videla, 2016), (24) (Moreno, 2004), (25) (Moreno et al., 2010), (26) (Pesce and Moreno, 2014), (27) (Abarzúa et al., 2004), (28) (Haberle and Bennett, 2004), (29) (Montade et al., 2013), (30) (Ashworth et al., 1991), (31) (Fesq-Martin et al., 2004), (32) (Lamy et al., 2010), centered at 53°S, (33) (Heusser et al., 2000), and (34) (Perren et al., 2025). See Sects. 5.3.1 to 5.3.5; Text S1 to S3 and Fig. S12 in the Supplementary Material for details. Error bars correspond to two standard deviations (2σ) calculated from the values reported in the Tables S5 and S6 (Läuchli et al., 2025, see Data availability). The gradient of blue shades in panel C schematically reflects the *core* and *peripheral* zone of the SWW belt as shown in Fig. 3.

5.3.1 Phase I (> 17 kyr BP)

Lower δ^2H_{wax} values before 17 ka BP imply a more northern position of the SWW *core* than today, with wetter conditions between 33°S and 36°S. Such conditions are consistent with wet and/or cold conditions previously inferred between 30°S and 36°S (Fig. 4, Flores-Aqueveque et al., 2021; Heusser et al., 2006a; Kaiser et al., 2008; Lamy et al., 1999; Valero-Garcés et al., 2005). The detection of slightly higher δ^2H_{wax} values at 30°S (Kaiser et al., 2024) indicating an influence of the *peripheral* zone of the SWW belt, and cold and dry conditions at 31°S (Zech et al., 2007) support reduced precipitation at ca. 30°S compared to the southern latitudes. This indicates an overall northern extent of SWW-driven precipitation during Phase I. Further south, previously published literature also confirm a northern influence of the SWW *core* with cold and wet conditions inferred between 40°S and 46°S (Fig. 4, e.g., Heusser et al., 2006b; Montade et al., 2013; Moreno et al., 2018; Moreno and León, 2003). The lower δ^2H_{wax} values at site OPD1233 (41°S, Kaiser et al., 2024) relative to the δ^2H_{wax} values recorded during the Holocene also implies a northern position of the SWW *core* (i.e., wetter conditions, Kaiser et al., 2024). Here, we locate the southern limit of the SWW *core* between 46°S and 53°S, as wet conditions were reconstructed at 46°S (Montade et al., 2013) and dry and cold conditions at 53°S (Heusser et al., 2000). This implies a wide SWW *core* extending between 33°S and at least 46°S during Phase I (Fig. 4).

5.3.2 Phase II (17 to 14 ka BP)

The southward migration of the SWW belt inferred from the decrease in δ^2H_{wax} records at 30°S and 33°S during Phase II implies a decrease in humidity recognized in most records along Chile. A gradual decreases in humidity was inferred from the grain-size distributions of site GeoB3375-1 between ca. 17 and 11 ka BP (27°S, Stuut and Lamy, 2004) and site GeoB7139-2 (30°S) between ca. 16 and 12 ka BP (Bernhardt et al., 2017; recalibrated to the new age-depth model). At 33°S, changes in clay assemblages, grain-sizes and sedimentation rates at the marine sites GIK 17748-2 and GeoB3302 also suggested gradually drier conditions after 18 ka BP (Lamy et al., 1999). At 34.5°S, dry conditions were reconstructed in Laguna Tagua Tagua between 17 and 15 ka BP (Valero-Garcés et al., 2005). At 36°S, a transition toward drier and warmer conditions was also inferred at ca. 17 ka BP (Heusser et al., 2006a; Muratli et al., 2010). However, relatively stable average δ^2H_{wax} values were recorded at site 22SL before 14.5 ka BP. The low response of site 22SL to the southward migration of the SWW belt is attributed here to the large scatter of the data, potentially masking low amplitude changes in the δ^2H_{wax} values, and/or a persistent influence of the SWW *core* in the source area of site 22SL. As both hypotheses nevertheless support an influence of SWW-driven precipitation in the source area of site 22SL during Phase II, we consider a southward migration of the SWW belt as the most likely scenario during this period.

Between 36°S and 46°S, the increase in the δ^2H_{wax} values at site OPD1233 (Fig. 5, 41°S, Kaiser et al., 2024), and the detection of drier and warmer conditions between ca. 17.8 ka BP and 14.8 ka BP (e.g., Montade et al., 2013; Moreno et al., 2018; Moreno and León, 2003; Moreno and Videla, 2016; Pesce and Moreno, 2014, further details in Fig. 4, Fig. S12 and Supplementary text S1 in the Supplementary Material) also imply a southward migration (or contraction, Kaiser et al., 2024) of the SWW belt. We also conclude to a southward migration of the southern limit of the SWW *core* between 49°S and 54°S as a transition from dry to wet conditions was detected at ca. 15.9 ka BP at 49°S (Ashworth et al., 1991) and at ca. 15.5 ka BP at 54°S (Heusser et al., 2000). Most records therefore confirm a southward migration of the SWW belt during Phase II.

5.3.3 Phase III (14 to 11.5 ka BP)

Increasing δ^2H_{wax} values in site GeoB7139-2 (Kaiser et al., 2024) and slightly decreasing values in site GeoB3304-5 during Phase III suggest a decoupling of the climate north and south of ca. 32°S. The increasing values at 30°S indicate an increasing influence of the SPH (Kaiser et al., 2024) consistent the drier conditions reconstructed by Bernhardt et al. (2017) and Stuut and Lamy (2004), and the influence of more local moisture spells inferred between 13 and 11.8 ka BP at 31.5°S by Ortega et al. (2012). The decreasing δ^2H_{wax} values at 33°S (GeoB3304-5) instead indicate a return northward of SWW-driven precipitation roughly consistent with the colder and/or wetter conditions reconstructed between 13.5 and 11.5 ka BP in Laguna Tagua Tagua (Valero-Garcés et al., 2005). Most records located between 40°S and 46°S also suggested colder and wetter conditions from ca. 14.8 ka BP and until 12.8 ka BP (e.g., Montade et al., 2013; Moreno et al., 2018; Pesce and Moreno, 2014, Fig. 4, Fig. S12 and Text S2 in the Supplementary Material for further references). This colder and wetter period was followed by a transition period characterized by slightly less precipitation and climate variability until ca. 11.5 ka BP (e.g., Montade et al., 2013; Moreno et al., 2018; Pesce and Moreno, 2014, Fig. 4, Fig. S12 and Text S2 in the Supplementary Material). Such transition period is however not detected in the δ^2H_{wax} records of site GeoB 3304-5 as our records only poorly cover this time interval. At site ODP 1233 (41°S, Kaiser et al., 2024), the stable values δ^2H_{wax} recorded during Phase III suggest that the northward migration of SWW-driven precipitation only weakly influenced δ^2H_{wax} records in the southern latitudes. During Phase III, we also locate the southern limit of the SWW *core* at around 54°S as relatively wet conditions were detected at ca. 53°C (Fesq-Martin et al., 2004), while a drier interval was suggested between ca. 14.8 and 12.8 ka BP at 54°S (Heusser et al., 2000). Overall, these findings confirm a northward migration of SWW-driven precipitation south of 32°S while progressively drier conditions prevailed north of this latitude between ca. 14 and 12 ka BP.

5.3.4 Phase IV (A and B, 11.5 to 5.5 ka BP)

The high δ^2H_{wax} values of sites GeoB7139-2 and GeoB3304-5 during Phase IV suggest the SPH (i.e., dry conditions) reached latitudes as far south as 33°S (Fig. 4 and Fig. S11 reported in the Supplementary Material). This agrees with the dry and warm conditions previously detected at 30°S (Kaiser et al., 2008; Muñoz et al., 2020, pollen moisture index). Between 32 and 35°S, several records also suggested dry conditions until 5.7 ka BP (Jenny et al., 2002a, 2003; Maldonado and Villagrán, 2006; Valero-Garcés et al., 2005; Villa-Martínez et al., 2003) and 4.2 ka BP (Maldonado and Villagrán, 2002), which confirms a southern extend of the SPH during Phase IV.

The δ^2H_{wax} values of site GeoB3304-5 (33°S) also showed some lower values between ca. 11 and 7 ka BP. This suggests temporary northward intrusions of SWW-driven precipitation that agrees with the sporadic precipitation events and wetter intervals detected between 11 and 8.5 ka BP from 31°S to 33°S (Jenny et al., 2002a, 2003; Maldonado et al., 2010; Maldonado and Villagrán, 2006; Ortega et al., 2012; Veit, 1996). An increase in the frequency of torrential rainfall was also identified between 8.6 and 6 ka BP in the sedimentological record of the Quebrada Santa Julia archeological site (31.5°S Ortega et al., 2012). This confirms the high sensitivity of site GeoB3304-5 to past δ^2H_{precip} values.

While predominantly dry and warm conditions prevailed north of 36°S, we recognize two distinct climate periods south of 36°S based on previously published literature. Most records between 40°S and 46°S suggested dry and warm conditions until 7.5 ka BP, after which colder and wetter conditions occurred (e.g., Abarzúa et al., 2004; Moreno et al., 2010, 2018; Pesce and Moreno, 2014, see Fig. 4, Fig. S12 and Text S3 in Supplementary Material for further references). This implies a northward migration of the SWW *core* at ca. 7.5 ka BP supported by the lower δ^2H_{wax} values recorded at ca. 8 ka BP in site ODP 1233 (Fig. 5, 41°S, Kaiser et al., 2024). Note however that an increase in the δ^2H_{wax} values of site ODP 1233 was then recorded until 5.5 ka BP (Kaiser et al., 2024) suggesting the latitudinal shift of the SWW *core* was only brief. During Phase IV, we locate the southern limit of the SWW *core* south of 56°S between ca. 10 and 7.5 ka BP as suggested by the wet conditions inferred by Perren et al. (2025). After ca. 7.5 ka BP, the SWW *core* likely migrated northward as drier conditions prevailed after 8.5 ka BP between 51°S and 53°S (Lamy et al., 2010) and after 7.5 ka BP at 56°S (Perren et al., 2025). Because of the pronounced climate changes detected at ca. 7.5 ka BP, we divided Phase IV into Phase IV A (11.5-7.5 ka BP) and B (7.5-5.5 ka BP). Mostly dry conditions prevailed as far south as 56°S during Phase IV A, while a decoupling of the climate north and south of 36°S marked Phase IV B, with dry conditions in the north and wet conditions in the south.

5.3.5 Phase V (last 5.5 kyr)

Decreasing δ^2H_{wax} values at sites GeoB7139-2 and GeoB3304-5 during Phase V suggest a northward migration of SWW-driven precipitation, implying progressively wetter conditions along Chile (Fig. 4 and Fig. S11 reported in the Supplementary Material). This agrees with the wetter conditions reconstructed at the Guanaqueros Bay (30°S) after around 5 ka BP (Muñoz et al., 2020, pollen moisture index) and the gradual increase in humidity reconstructed between ca. 5.7 and 4.2 ka BP at the Palo Colorado swamp forest (32°S; Maldonado and Villagrán, 2006), and between 5.7 and 3.2 ka BP at Laguna Aculeo (33°S;

Jenny et al., 2002a; Villa-Martínez et al., 2003). At Laguna Aculeo, higher lake levels were furthermore reconstructed after 6 ka BP (Jenny et al., 2003). A minor change in sediment provenance suggesting a transition toward wetter conditions, and a more variable climate was also detected at around 5 ka BP in the record of site GIK 17748-2 (33°S; Lamy et al., 1999). This contrasts with the record of the Lago Vichuqué at 34.5°S indicating a stronger influence of the SPH between 6.2 and 4 ka BP (Frugone-Álvarez et al., 2017). Yet, as most records suggests an earlier increase in humidity, we consider an onset of the northward migration of SWW-driven precipitation at ca. 5.5 ka BP more likely.

The high variability of the δ^2H_{wax} *n*-C_{29} values at site GeoB3304-5 furthermore indicates some climate variability at ca. 4 ka BP, in line with short-term drought and flood events inferred at the Palo Colorado swamp forest after 4.2 ka BP (32°S, Maldonado and Villagrán, 2006) and at Laguna Aculeo after 3 ka BP (33°S, Jenny et al., 2002a, b, 2003; Villa-Martínez et al., 2003, 2004). Similar climate variability was also detected in Southern Chile.

Between 40°S and 46°S , the wet conditions inferred at ca 7.5 ka BP persisted over the last 5.5 kyr (Fig. 4, Abarzúa et al., 2004; Haberle and Bennett, 2004; Jara and Moreno, 2014; Montade et al., 2013; Moreno, 2004; Moreno et al., 2010, 2018; Moreno and León, 2003; Pesce and Moreno, 2014; Vargas-Ramirez et al., 2008) and progressively led to modern climate (Haberle and Bennett, 2004; Montade et al., 2013; Moreno et al., 2010). This agrees with the northward expansion of the SWW belt previously suggested by the δ^2H_{wax} record of site ODP1233 (Fig. 5, Kaiser et al., 2024). Superimposed on this progressive increase in precipitation, several records suggested the occurrence of drier (e.g., droughts) and wetter intervals at centennial to millennial timescales (Abarzúa et al., 2004; Haberle and Bennett, 2004; Jara and Moreno, 2012, 2014; Moreno, 2004; Moreno and Videla, 2016; Pesce and Moreno, 2014; Vargas-Ramirez et al., 2008). This confirms an overall high climate variability along Chile during Phase V.

During Phase V, we locate the southern limit of the SWW *core* between 53°S and 49°S as dry conditions characterized the last 5.5 ka BP between 51°S and 53°S (Lamy et al., 2010), while a return to wetter conditions was inferred after 3 ka BP at 49°S (Ashworth et al., 1991). Considering these findings, we conclude to a northward migration of SWW-driven precipitation, associated with shorter-term climate variability, as the most likely scenario during Phase V.

5.4 Atmospheric pathways of the South American West Coast since the LGM

To investigate the dynamic feedbacks between the climate systems of the west coast of South America, we report and compare the past latitudinal extent of the ITCZ to past latitudes of the SPH and the SWW belt. This allows identifying the dominant large-scale atmospheric circulation pathways (or teleconnections) over the last 20 kyr.

At present, the main atmospheric pathways between tropical and extratropical latitudes in South America are mainly attributed to stationary Rossby wave trains – atmospheric pressure anomalies extending toward the poles (e.g., Mo and Paegle, 2001; Rutllant and Fuenzalida, 1991) – generated by convection at the tropics mainly related to ENSO events (ENSO-atmospheric teleconnections; Cai et al., 2020; Mo and Paegle, 2001; Montecinos and Aceituno, 2003; Rutllant and Fuenzalida, 1991; Turner, 2004; Yeh et al., 2018). Two main atmospheric pathways emerge during ENSO. During the positive phase of ENSO (El-Niño), warm SST anomalies and a southward-shifted ITCZ (Schneider et al., 2014) are often associated, through Rossby wave trains, with a positive pressure anomaly over the Amundsen and Bellingshausen Seas, and intensified Hadley cells shifted equatorward in the central Pacific (Li et al., 2023; Oort and Yienger, 1996). This leads to an equatorward displacement of the SPH and a strengthening of the subtropical jet (Cai et al., 2020; Turner, 2004; Yuan et al., 2018) implying enhanced precipitation in central Chile (e.g., Montecinos and Aceituno, 2003; Yeh et al., 2018). El-Niño-like teleconnections are thus mainly associated with a southward and northward position of the ITCZ and SWW belt, respectively. The opposite situation tends to prevail during La Niña events (e.g, Campos and Rondanelli, 2023; Sinclair et al., 1997). Cold SST anomalies in the tropical Pacific and a northward-shifted ITCZ are then often associated with a weakened subtropical jet (i.e., a strengthened mid-latitude jet) leading to a decrease in precipitation amounts in central Chile. La-Niña events are thus mainly associated with a northward and southward position of the ITCZ and SWW belt, respectively. During ENSO events, the strength of the Hadley cell is mainly controlled by the energy flux at the tropic (Schneider et al 2014).

As ENSO events are responsible for most of the modern interannual climate variability on the west coast of South America (Garreaud, 2009; Zhang et al., 2022), no details are given on the atmospheric pathways associated with other modern climate phenomena such as the Madden–Julian Oscillation or the Pacific Decadal Oscillation (Reboita et al., 2021; Zhang et al., 2022). Note however that these phenomena can interfere with the atmospheric pathways associated with ENSO (Yuan et al., 2018). For instance, during negative ENSO-SAM correlation (e.g., El-Niño and a negative SAM, Sect. 2.2, Fogt et al., 2011) – the most frequently observed correlation in recent climate (Carvalho et al., 2005; Dätwyler et al., 2020; Kim et al., 2017) – the above-described ENSO-atmospheric pathways are more frequent. Conversely, when the ENSO-SAM cycles are positively correlated (e.g., La Niña and a negative SAM), these tend to be reduced (Dätwyler et al., 2020; Fogt et al., 2011; Fogt and Bromwich, 2006).

Different atmospheric pathways have been invoked to explain past climate, in which the migration of the ITCZ to the warmer hemisphere – associated with large interhemispheric thermal gradient and cross equatorial heat transport from the warmer to the colder hemisphere (Bjerknes, 1964; Bordoni and Schneider, 2008; Broccoli et al., 2006; Geen et al., 2020; Schneider et al., 2014) is thought to weaken the Hadley cell in the hemisphere to which it migrates (Broccoli et al., 2006; Ceppi et al., 2013; Chiang et al., 2014; Chiang and Bitz, 2005; Chiang and Friedman, 2012; Lee et al., 2011; Lindzen and Hou, 1988; Prohaska et al., 2023). A weakening of the Hadley cell, in turn, results in a weaker subtropical jet and a shift southward of the Westerlies storm tacks, and vice versa (Ceppi et al., 2013; Chiang et al., 2014; Lee et al., 2011; Lindzen and Hou, 1988). Such climate conditions resemble modern seasonal climate changes and imply a southern position of the ITCZ associated with a southern position of the SWW belt, and vice versa. These atmospheric pathways were mainly invoked to explain past climate associated with abrupt changes in interhemispheric temperature (e.g., Chiang et al., 2014; Lee et al., 2011).

Considering the control exerted by the above-mention atmospheric pathways on climate, any changes in the leading atmospheric pathway regime should be reflected by changes in hydroclimate along the west coast of South America. We thus use our reconstruction of the SWW belt, compared to the past latitudes of the ITCZ, to identify dominant atmospheric pathways influencing the South American climate during the last 20 kyr. Note that our approach is based exclusively on the relationship detected between the SWW belt and the ITCZ along the west coast of South America, whereas atmospheric pathways or teleconnections act at a larger scale. Future research should thus focus on investigating the consistency between our reconstruction of atmospheric pathways and climate at other locations.

5.4.1 Last Glacial Maximum: Phase I (>17 ka BP)

During Phase I, The ITCZ was located south of its modern position (Fig. 5 and Fig. S13 reported in the Supplementary Material, Arbuszewski et al., 2013; Koutavas et al., 2002; Koutavas and Lynch-Stieglitz, 2004; Reimi and Marcantonio, 2016; Yuan et al., 2023) and the SWW belt extended as far north as at least 30°S. Such southern and northern positions for the ITCZ and the SWW belt, respectively, imply a contracted Hadley cell consistent with the lack of evidences for a signal of the SPH at the studied sites. A southward ITCZ is furthermore consistent with a colder NH relative to the SH during the LGM (e.g., Annan et al., 2022; Osman et al., 2021; Shi et al., 2023). Yet, considering the mechanisms described by Lee et al. (2011), Ceppi et al. (2013) or Chiang et al. (2014), such conditions also imply a weaker subtropical jet and a shift southward of the SWW belt not observed. The northern position of the SWW belt during the LGM thus suggests that mechanisms differing from the above-mentioned ones might have acted on the climate during this period. Further in-depth investigation of climate under the conditions of an ice age – not acquired within the scope of this study – are needed to explain the observed conditions.

5.4.2 The deglaciation period: Phase II and III (17 – 11.5 ka BP)

During the deglaciation period (Phase II and III, ca. 17-11.5 ka BP), the climate conditions along the west coast of South America are consistent with the atmospheric pathways associated with large changes in interhemispheric thermal gradients and a modulation of the Hadley cell circulation (e.g., Chiang et al., 2014; Lee et al., 2011). During Phase II (17-14 ka BP, roughly corresponding to the Heinrich Stadial I), the southward shift of the SWW belt inferred here is coeval with a southward position of the ITCZ (Fig. 5; Arbuszewski et al., 2013; Deplazes et al., 2013; Yuan et al., 2023). During Phase III (14-11.5 ka BP), the δ^2H records – mainly covering the period of the Antarctic Cold Reversal (ACR; 14.7 to 13 ka BP; Pedro et al., 2016) – then indicate a northward shift of the SWW belt coeval with a northward shift of the ITCZ (Fig. 5; Deplazes et al., 2013; Pedro et al., 2016; Yuan et al., 2023). Here, the southward shift of the ITCZ during Heinrich Stadial 1 (northward during the ACR) likely caused a reduction (strengthening) of the SH Hadley cell in turn weakening (enhancing) the subtropical jet and strengthening (weakening) the mid-latitude jet (Chiang et al., 2014; Lee et al., 2011; Pedro et al., 2018). We furthermore detect a decoupling between north and south of 32°S during the ACR – confirmed at larger scale by Pedro et al. (2016) – possibly resulting from a stronger subtropical jet and the blocking of the SWW belt by the stronger subsidence of the air masses of the Hadley cell (i.e., a stronger SPH). These climate conditions thus directly follow the mechanisms described by Lee et al. (2011) and Chiang et al. (2014).

During the Younger Dryas (YD, 12.9-11.6 ka BP), a southward shift of the ITCZ is detected (Fig. 5; Deplazes et al., 2013; Haug et al., 2001b) and reduced precipitation inferred in some records between 40°S and 46°S (Montade et al., 2013; e.g., Moreno et al., 2018; Moreno and León, 2003) suggests a southward shift of the SWW. These reconstructions are in line with an influence of the atmospheric pathways resulting from large interhemispheric temperature gradients. Some uncertainties are however associated with this period as not well-covered by the δ^2H data. Nevertheless, current results suggest that climate was controlled by changes in interhemispheric thermal gradients during the entire deglaciation period.

Consensus exists on the predominant role of the interhemispheric thermal gradient on large-scale oceanic and atmospheric circulation changes during the deglaciation period (Fig. 5, Osman et al., 2021; Shakun et al., 2012). During Phase II, the southward positions of the ITCZ and the SWW belt are consistent with large temperature differences between the hemispheres, with a colder NH relative to the SH (Bjerknes, 1964; Osman et al., 2021; Pedro et al., 2018; Schneider et al., 2014; Shakun et al., 2012), resulting from a reduced AMOC (Crowley, 1992; McManus et al., 2004; Moreno-Chamarro et al., 2019; Pedro et al., 2016, 2018; Pöppelmeier et al., 2023b). During the Bølling-Allerød interstadial period (or ACR), the northward migration of the ITCZ is also in line with a decrease in interhemispheric thermal gradient caused by the relative warming of the NH compared to the SH (Fig. 5, Deplazes et al., 2013; Osman et al., 2021; Pedro et al., 2016; Shakun et al., 2012; Yuan et al., 2023) associated with a strengthened AMOC (e.g., McManus et al., 2004; Pöppelmeier et al., 2023b). During the YD, the shift southward of the ITCZ then agrees with the cooling of the NH, relative to the SH, increasing the temperature differences between the hemispheres (Shakun et al., 2012) associated with a reduced AMOC (Fig. 5; Deplazes et al., 2013; Haug et al., 2001b). The consistency between the change in interhemispheric temperature and the response of the ITCZ and the SWW belt confirm the role of the mechanisms described, among others, by Lee et al. (2011) and Chiang et al. (2014) on the climate of the west coast of South America during the deglaciation period.

5.4.3 The Holocene (Phase IV A and B, 11.5- 5.5 ka BP and Phase V, 5.5 ka BP-present)

During the Holocene, insolation is considered the main forcing of climate as stable AMOC strength (Lippold et al., 2019; McManus et al., 2004; Pöppelmeier et al., 2023b) stable atmospheric CO_2 concentrations (Köhler et al., 2017a; Monnin, 2006), and small temperature difference between the hemispheres characterize this period (Fig. 5; Erb et al., 2022b; Osman et al., 2021; Shakun et al., 2012). Specifically, lower summer insolation is recorded in the SH relative to the NH during the early Holocene (Phase IV A, Fig.. 5, Berger, 1988) likely causing a relative cooling of the SH, whereas the opposite conditions prevail during the late Holocene (Phase V). Furthermore, at the late Holocene, the relative warming of the NH compared to the SH was likely enhanced by the larger proportion of landmasses in the NH compared to the SH, responding faster to temperature changes than oceans (e.g., Byrne and O'Gorman, 2013; Joshi et al., 2008). The transition between these two periods (mid-Holocene, between Phase IV B and V) was characterized by lower seasonality (Berger, 1988). Distinct climate conditions were detected over the Holocene, suggesting different atmospheric pathways marked this epoch.

During most of the early and late Holocene (Phase IV A and V), a relationship is detected between the climate conditions, changes in insolation and the atmospheric pathways associated with ENSO (see above). During Phase IV A (11.5-7.5 ka BP), a northward position of the ITCZ (Fig. 5; Arbuszewski et al., 2013; Haug et al., 2001b; Koutavas et al., 2006; Reimi and Marcantonio, 2016; Schneider et al., 2014; Yuan et al., 2023), consistent with lower summer insolation in the SH relative to the NH, is associated with a southward SWW belt (Sect. 5.3.4). These conditions resemble La-Niña events and/or a positive SAM phase also inferred elsewhere in South America during the same period (Carré et al., 2012; Jenny et al., 2002a; Koutavas et al., 2002; Ortega et al., 2012; Vargas et al., 2006). During the last 5.5 ka BP (Phase V, late Holocene), the opposite conditions prevailed. The ITCZ was progressively shifted southward (Fig. 5, Haug et al., 2001b; Schneider et al., 2014; Yuan et al., 2023), reflecting the progressive increase in summer insolation in the SH relative to the NH, while the SWW belt gradually migrated northward (Sect. 5.3.5). This progressive onset of El-Niño-like conditions (and/or a negative SAM) aligns with previously publish studies (Haug et al., 2001b; Jenny et al., 2002a; Lamy et al., 2010; Ortega et al., 2019; Sandweiss et al., 1996; Vargas et al., 2006) and the detection of muted ENSO conditions during the mid-Holocene (ca. 5-3 ka BP, e.g., Chen et al., 2016; Emile-Geay et al., 2016; Koutavas and Joanides, 2012). This confirms a predominant role of ENSO in setting the climate of the Holocene and highlights the major role of precession cycles (i.e., insolation, Lamy et al., 2019) in setting the climate of the west coast of South America during the Holocene.

Between 7.5 and 5.5 ka BP (Phase IV B), the climate mechanisms however remain unclear. Both the ITCZ and the SWW *core* are then located northward, which resemble the climate conditions of the ACR (see above). Yet, a small interhemispheric thermal gradient mark this period (Fig. 5, Erb et al., 2022b). Both atmospheric pathways associated with ENSO and those resulting from large interhemispheric thermal gradients therefore cannot explain these climate conditions. Furthermore, time lags are detected between the northward migration of the SWW *core* at ca. 7.5 ka BP and the short-term decrease in the AMOC strength associated with the NH 8.2 ka BP cooling event (e.g., Renssen et al., 2001; Thomas et al., 2007), the lower seasonality detected at ca. 6 ka BP (Fig. 5, Berger, 1988) and muted-ENSO detected between ca. 5 and 3 ka BP (see above). Here, we hypothesize that Phase IV B climate could result from a positive ENSO-SAM correlation attributed in recent climate to internal forcings (Dätwyler et al., 2020). This agrees with La Niña-like conditions detected north of 36°S (this study, Carré et al., 2012, 2014; Salvatteci et al., 2019; Vargas et al., 2006), while the latitudes south of 36°S resembled El-Niño conditions and/or a negative SAM phase. We however consider that further in-depth investigation, not performed within the scope of this study, are needed to understand further such correlations in the climate context of Phase IV B.

https://doi.org/10.5194/egusphere-2025-3153
Preprint. Discussion started: 10 July 2025

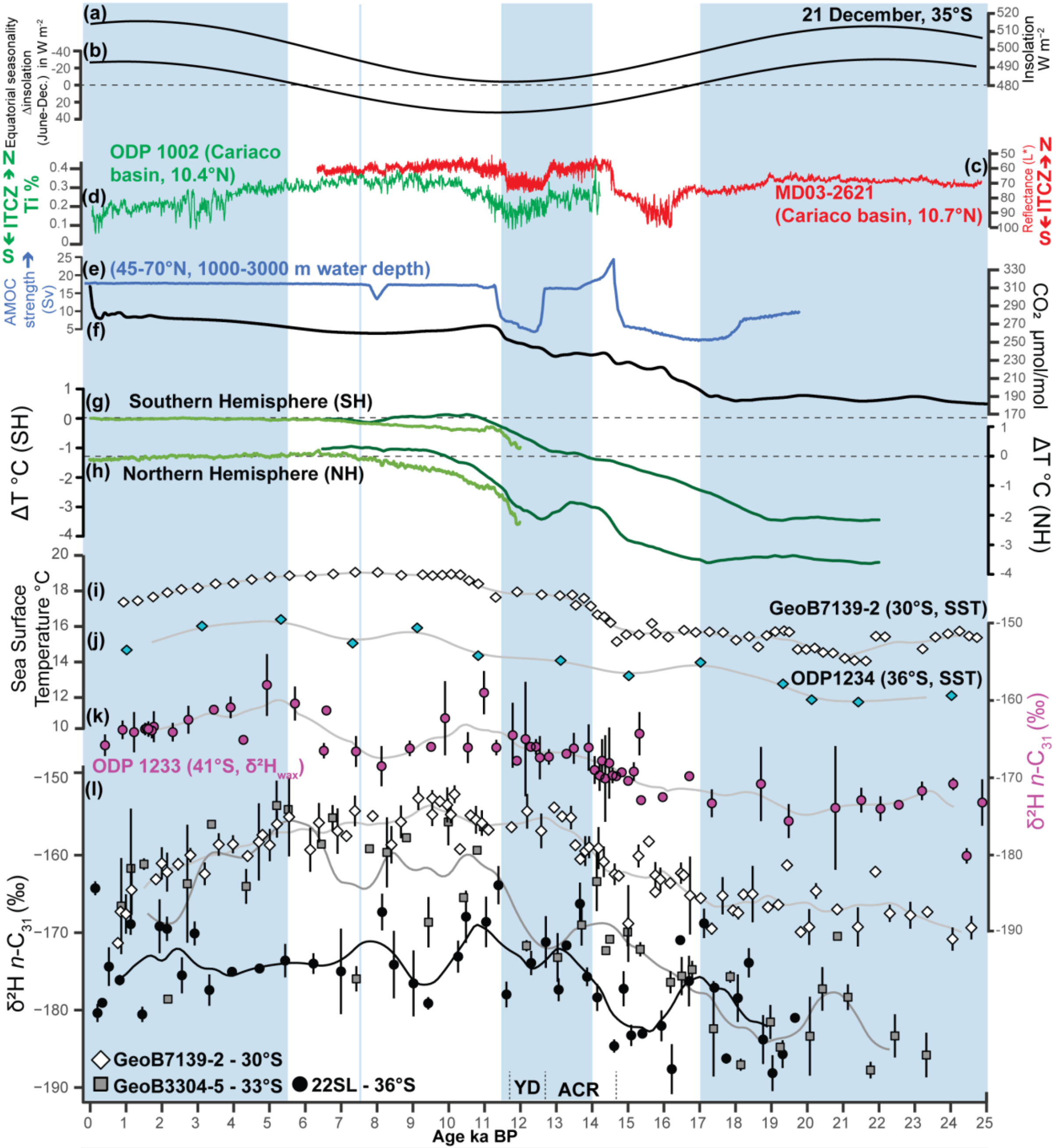

Phase	V	IVB	IVA	III-YD III-ACR	II	I
Age	5 kyr BP - Present	7 - 5 kyr BP	11.5 - 7 kyr BP	14 - 11.5 kyr BP	17 - 14 kyr BP	>17 kyr BP
ITCZ	migration South	North	North	South North	migr. further South	South of modern position
SWW	migration North	North	South	? North	migr. further South	North of modern position
Atm. path.	ENSO (El-Niño)	?	ENSO (La-Niña)	ΔT hemisph.	ΔT hemisph.	?

https://doi.org/10.5194/egusphere-2025-3153
Preprint. Discussion started: 10 July 2025

Figure 5 Comparison of the leaf-wax *n*-alkane hydrogen isotope records (*n*-C_{31}, l) to past changes in insolation (a), seasonality (b) and independent paleoenvironmental records (c-k). (a) Equatorial seasonality modelled as the difference in insolation between June and December at the equator (Berger, 1988; Berger and Loutre, 1991). (b) Past insolation during the austral summer at the latitude of 35°S (Berger, 1988; Berger and Loutre, 1991). (c) Reflectance at site MD03-2621 indicating past latitudinal migrations of the ITCZ (Deplazes et al., 2013). (d) Titanium content of site ODP 1002 indicating past latitudinal migrations of the ITCZ (Haug et al., 2001b, a). (e) AMOC strength derived from the model of Pöppelmeier et al. (2023b, a) for the North Atlantic (45-70°N) between 1000 and 3000 m water depth. (f) Continuous record of atmospheric CO_2 (spline-smoothed data) compiled by Köhler et al. (2017a, b). (g) Southern Hemisphere surface temperature from Shakun et al. (2012, dark green) and Erb et al. (2022b, a, light green) reported as temperature difference to pre-industrial values (ΔT). (h) Northern Hemisphere surface temperature from Shakun et al. (2012, dark green) and Erb et al. (2022b, a, light green) reported as temperature difference to pre-industrial values (ΔT). (i) Sea surface temperature ($U^{k'}_{37}$, SST) at site GeoB7139-2 (30°S, Kaiser et al., 2008, 2024). (j) Sea surface temperature ($U^{k'}_{37}$, SST) at site ODP 1234 (36°S, de Bar et al., 2018a, b). (k) δ^2H_{wax} (*n*-C_{31}) record of site ODP 1233 (41°S, Kaiser et al., 2024). (l) δ^2H_{wax} (*n*-C_{31}) record of sites GeoB7139-2 (30°S, Kaiser et al., 2024), GeoB3304-5 (33°S) and 22SL (36°S). Error bars in (l) represent two standard deviations (2σ) calculated from the values reported in Tables S5 and S6 (Läuchli et al., 2025, see Data availability).

6 Conclusion

This study provides a new, high-resolution reconstruction of past hydrological regimes along Chile over the last 20,000 years, based on δ^2H_{wax} records from marine sediments at key latitudes spanning the interface between the Southern Westerly Wind (SWW) belt and the Subtropical Pacific High (SPH). Our results suggest that central Chile was marked by wet conditions during the Last Glacial Maximum, after which increasingly drier conditions, partly interrupted during the Antarctic Cord Reversal, marked the deglaciation period. During the early Holocene, dry conditions characterized central Chile that were replaced, at ca. 7.5 ka BP and south of 36°S, by wetter conditions. A gradual increase in moisture then marked central Chile over the last 5.5 kyr. Our reconstruction indicates a southward migration of the SWW belt during the deglaciation period, briefly interrupted during the Antarctic Cold Reversal. During the early Holocene, the SWW belt and the SPH reached their southernmost latitudes, after which a displacement northward was detected at ca. 7.5 ka BP for the SWW-*core*. The late Holocene was then marked by a progressive northward shift of the SWW belt. By integrating these new δ^2H_{wax} records with reconstructions of past ITCZ positions, we identify major shifts in circulation regimes.

Our reconstruction, combined with past reconstructions of the ITCZ, allow identifying two dominant atmospheric pathways modulating the climate of the west coast of South America since the LGM. Atmospheric pathways driven by large interhemispheric temperature contrasts and changes in the strength of Hadley cells likely prevailed during the last deglaciation period, while, atmospheric pathways associated with ENSO likely dominated during the Holocene, except between 7.5 and 5.5 ka BP. These shifts correspond to changing dominance of major forcings: Atlantic Meridional Overturning Circulation (AMOC) and hemispheric temperature contrasts during the deglaciation period, and orbital insolation forcing (precession) during most of the Holocene. This work highlights the value of δ^2H_{wax} records for unraveling complex hydroclimate patterns and underscores the need for further constraints on large-scale atmospheric pathways to deconvolve past Earth's climate.

Data availability

All data generated or analysed during this study (Table S1 to S8) can be found in the following GFZ Data Services repository (Läuchli et al., 2025)
Review link:
https://dataservices.gfz-potsdam.de/panmetaworks/review/4a3d7c9d56459440ad3e3c94dd66c5cedb89015bf859c30e3a25f8077d7993b4/
The repositories will be made publicly available upon publication.

Sample availability

The samples with IGSN stored at the GFZ Helmholtz Centre for Geosciences are listed in the data publication (see Data availability).

Acknowledgments

This research was funded by the DFG grants BE 5070/6-1 (to AB), WI 3874/7-1 (to HW) and SA1889/3-1 (to DS) as part of the German Science Foundation (DFG) priority program SPP-1803 "EarthShape: Earth Surface Shaping by Biota". The MARUM Research Center (Bremen) provided the GeoB cores samples and the 22SL Gravity Core was provided by the Bundesanstalt für Geowissenschaften und Rohstoffe (BGR, Hannover). We thank the Chilean National Park Service (CONAF) for providing on-site support of our research. We thank Esteban Andrés Rodríguez Sepúlveda for help with sampling rivers and Oliver Rach, Emily Ikawi and Gero Fischer for support with lab work.

Author contributions

CL: conceptualization, data curation, methodology, supervision, formal analysis, investigation, validation, visualisation, project administration, writing original draft, review and editing. NGL: formal analysis, investigation, writing reviews. AB: conceptualization, funding acquisition, project administration, resources, supervision, writing reviews. HW: conceptualization, funding acquisition, writing reviews. PF: conceptualization, writing reviews. MM: resources, writing reviews. AL resources, writing reviews. DS: conceptualization, funding acquisition, project administration, resources, supervision, writing reviews.

Conflict of interest

The authors declare that they have no conflict of interest.

References

Abarzúa, A. M., Villagrán, C., and Moreno, P. I.: Deglacial and postglacial climate history in east-central Isla Grande De Chiloé, Southern Chile (43°S), Quat. Res., 62, 49–59, https://doi.org/10.1016/j.yqres.2004.04.005, 2004.

Aitchison, J.: The Statistical Analysis of Compositional Data, J. R. Stat. Soc. Ser. B Methodol., 44, 139–160, https://doi.org/10.1111/j.2517-6161.1982.tb01195.x, 1982.

Aitchison, J.: A Concise Guide to Compositional Data Analysis, Compos. Data Anal. Workshop, 2005.

Ancapichún, S. and Garcés-Vargas, J.: Variability of the Southeast Pacific Subtropical Anticyclone and its impact on sea surface temperature off north-central Chile, Cienc. Mar., 41, 1–20, https://doi.org/10.7773/cm.v41i1.2338, 2015.

Annan, J. D., Hargreaves, J. C., and Mauritsen, T.: A new global surface temperature reconstruction for the Last Glacial Maximum, Clim. Past, 18, 1883–1896, https://doi.org/10.5194/cp-18-1883-2022, 2022.

Arbuszewski, J. A., deMenocal, P. B., Cléroux, C., Bradtmiller, L., and Mix, A.: Meridional shifts of the Atlantic intertropical convergence zone since the Last Glacial Maximum, Nat. Geosci., 6, 959–962, https://doi.org/10.1038/ngeo1961, 2013.

Ashworth, A. C., Markgraf, V., and Villagran, C.: Late Quaternary climatic history of the Chilean Channels based on fossil pollen and beetle analyses, with an analysis of the modern vegetation and pollen rain, J. Quat. Sci., 6, 279–291, https://doi.org/10.1002/jqs.3390060403, 1991.

Bailey, A., Posmentier, E., and Feng, X.: Patterns of Evaporation and Precipitation Drive Global Isotopic Changes in Atmospheric Moisture, Geophys. Res. Lett., 45, 7093–7101, https://doi.org/10.1029/2018GL078254, 2018.

Bals-Elsholz, T. M., Atallah, E. H., Bosart, L. F., Wasula, T. A., Cempa, M. J., and Lupo, A. R.: The Wintertime Southern Hemisphere Split Jet: Structure, Variability, and Evolution, J. Clim., 14, 4191–4215, https://doi.org/10.1175/1520-0442(2001)014<4191:TWSHSJ>2.0.CO;2, 2001.

de Bar, M. W., Stolwijk, D. J., McManus, J. F., Sinninghe Damsté, J. S., and Schouten, S.: A Late Quaternary climate record based on long-chain diol proxies from the Chilean margin, Clim. Past, 14, 1783–1803, https://doi.org/10.5194/cp-14-1783-2018, 2018a.

de Bar, M. W., Stolwijk, D., McManus, J. F., Sinninghe Damsté, J. S., and Schouten, S.: Organic geochemistry of ODP Site 202-1234, https://doi.org/10.1594/PANGAEA.892651, 2018b.

Barrett, B. S. and Hameed, S.: Seasonal Variability in Precipitation in Central and Southern Chile: Modulation by the South Pacific High, J. Clim., 30, 55–69, https://doi.org/10.1175/JCLI-D-16-0019.1, 2017.

Barrett, B. S., Garreaud, R., and Falvey, M.: Effect of the Andes Cordillera on Precipitation from a Midlatitude Cold Front, Mon. Weather Rev., 137, 3092–3109, https://doi.org/10.1175/2009MWR2881.1, 2009.

Berger, A.: Milankovitch Theory and climate, Rev. Geophys., 26, 624–657, https://doi.org/10.1029/RG026i004p00624, 1988.

Berger, A. and Loutre, M. F.: Insolation values for the climate of the last 10 million years, Quat. Sci. Rev., 10, 297–317, https://doi.org/10.1016/0277-3791(91)90033-Q, 1991.

https://doi.org/10.5194/egusphere-2025-3153
Preprint. Discussion started: 10 July 2025

Bernhardt, A., Melnick, D., Hebbeln, D., Lückge, A., and Strecker, M. R.: Turbidite paleoseismology along the active continental margin of Chile – Feasible or not?, Quat. Sci. Rev., 120, 71–92, https://doi.org/10.1016/j.quascirev.2015.04.001, 2015.

Bernhardt, A., Schwanghart, W., Hebbeln, D., Stuut, J.-B. W., and Strecker, M. R.: Immediate propagation of deglacial environmental change to deep-marine turbidite systems along the Chile convergent margin, Earth Planet. Sci. Lett., 473, 190–204, https://doi.org/10.1016/j.epsl.2017.05.017, 2017.

Bi, X., Sheng, G., Liu, X., Li, C., and Fu, J.: Molecular and carbon and hydrogen isotopic composition of n-alkanes in plant leaf waxes, Org. Geochem., 36, 1405–1417, https://doi.org/10.1016/j.orggeochem.2005.06.001, 2005.

Bjerknes, J.: Atlantic Air-Sea Interaction, in: Advances in Geophysics, vol. 10, edited by: Landsberg, H. E. and Van Mieghem, J., Elsevier, 1–82, https://doi.org/10.1016/S0065-2687(08)60005-9, 1964.

Blaauw, M. and Christen, J. A.: Flexible paleoclimate age-depth models using an autoregressive gamma process, Bayesian Anal., 6, 457–474, https://doi.org/10.1214/11-BA618, 2011.

Bordoni, S. and Schneider, T.: Monsoons as eddy-mediated regime transitions of the tropical overturning circulation, Nat. Geosci., 1, 515–519, https://doi.org/10.1038/ngeo248, 2008.

Bowen, G. J. and Revenaugh, J.: Interpolating the isotopic composition of modern meteoric precipitation, Water Resour. Res., 39, https://doi.org/10.1029/2003WR002086, 2003.

Bowen, G. J., Wassenaar, L. I., and Hobson, K. A.: Global application of stable hydrogen and oxygen isotopes to wildlife forensics, Oecologia, 143, 337–348, https://doi.org/10.1007/s00442-004-1813-y, 2005.

Bowen, G. J., Cai, Z., Fiorella, R. P., and Putman, A. L.: Isotopes in the Water Cycle: Regional- to Global-Scale Patterns and Applications, Annu. Rev. Earth Planet. Sci., 47, 453–479, https://doi.org/10.1146/annurev-earth-053018-060220, 2019.

Broccoli, A. J., Dahl, K. A., and Stouffer, R. J.: Response of the ITCZ to Northern Hemisphere cooling, Geophys. Res. Lett., 33, https://doi.org/10.1029/2005GL024546, 2006.

Byrne, M. P. and O'Gorman, P. A.: Link between land-ocean warming contrast and surface relative humidities in simulations with coupled climate models, Geophys. Res. Lett., 40, 5223–5227, https://doi.org/10.1002/grl.50971, 2013.

Cai, W., McPhaden, M. J., Grimm, A. M., Rodrigues, R. R., Taschetto, A. S., Garreaud, R. D., Dewitte, B., Poveda, G., Ham, Y.-G., Santoso, A., Ng, B., Anderson, W., Wang, G., Geng, T., Jo, H.-S., Marengo, J. A., Alves, L. M., Osman, M., Li, S., Wu, L., Karamperidou, C., Takahashi, K., and Vera, C.: Climate impacts of the El Niño–Southern Oscillation on South America, Nat. Rev. Earth Environ., 1, 215–231, https://doi.org/10.1038/s43017-020-0040-3, 2020.

Campos, D. and Rondanelli, R.: ENSO-Related Precipitation Variability in Central Chile: The Role of Large Scale Moisture Transport, J. Geophys. Res. Atmospheres, 128, e2023JD038671, https://doi.org/10.1029/2023JD038671, 2023.

Carré, M., Azzoug, M., Bentaleb, I., Chase, B. M., Fontugne, M., Jackson, D., Ledru, M.-P., Maldonado, A., Sachs, J. P., and Schauer, A. J.: Mid-Holocene mean climate in the south eastern Pacific and its influence on South America, Quat. Int., 253, 55–66, https://doi.org/10.1016/j.quaint.2011.02.004, 2012.

Carré, M., Sachs, J. P., Purca, S., Schauer, A. J., Braconnot, P., Falcón, R. A., Julien, M., and Lavallée, D.: Holocene history of ENSO variance and asymmetry in the eastern tropical Pacific, Science, 345, 1045–1048, https://doi.org/10.1126/science.1252220, 2014.

Carvalho, L. M. V., Jones, C., and Ambrizzi, T.: Opposite Phases of the Antarctic Oscillation and Relationships with Intraseasonal to Interannual Activity in the Tropics during the Austral Summer, J. Clim., 18, 702–718, https://doi.org/10.1175/JCLI-3284.1, 2005.

Ceppi, P., Hwang, Y.-T., Liu, X., Frierson, D. M. W., and Hartmann, D. L.: The relationship between the ITCZ and the Southern Hemispheric eddy-driven jet, J. Geophys. Res. Atmospheres, 118, 5136–5146, https://doi.org/10.1002/jgrd.50461, 2013.

Chen, S., Hoffmann, S. S., Lund, D. C., Cobb, K. M., Emile-Geay, J., and Adkins, J. F.: A high-resolution speleothem record of western equatorial Pacific rainfall: Implications for Holocene ENSO evolution, Earth Planet. Sci. Lett., 442, 61–71, https://doi.org/10.1016/j.epsl.2016.02.050, 2016.

Chiang, J. C. H. and Bitz, C. M.: Influence of high latitude ice cover on the marine Intertropical Convergence Zone, Clim. Dyn., 25, 477–496, https://doi.org/10.1007/s00382-005-0040-5, 2005.

Chiang, J. C. H. and Friedman, A. R.: Extratropical Cooling, Interhemispheric Thermal Gradients, and Tropical Climate Change, Annu. Rev. Earth Planet. Sci., 40, 383–412, https://doi.org/10.1146/annurev-earth-042711-105545, 2012.

Chiang, J. C. H., Lee, S.-Y., Putnam, A. E., and Wang, X.: South Pacific Split Jet, ITCZ shifts, and atmospheric North–South linkages during abrupt climate changes of the last glacial period, Earth Planet. Sci. Lett., 406, 233–246, https://doi.org/10.1016/j.epsl.2014.09.012, 2014.

Collins, J. A., Schefuß, E., Mulitza, S., Prange, M., Werner, M., Tharammal, T., Paul, A., and Wefer, G.: Estimating the hydrogen isotopic composition of past precipitation using leaf-waxes from western Africa, Quat. Sci. Rev., 65, 88–101, https://doi.org/10.1016/j.quascirev.2013.01.007, 2013.

Crowley, T. J.: North Atlantic Deep Water cools the southern hemisphere, Paleoceanography, 7, 489–497, https://doi.org/10.1029/92PA01058, 1992.

Dansgaard, W.: Stable isotopes in precipitation, Tellus, 16, 436–468, https://doi.org/10.3402/tellusa.v16i4.8993, 1964.

Dätwyler, C., Grosjean, M., Steiger, N. J., and Neukom, R.: Teleconnections and relationship between the El Niño–Southern Oscillation (ENSO) and the Southern Annular Mode (SAM) in reconstructions and models over the past millennium, Clim. Past, 16, 743–756, https://doi.org/10.5194/cp-16-743-2020, 2020.

De Pol-Holz, R., Keigwin, L., Southon, J., Hebbeln, D., and Mohtadi, M.: No signature of abyssal carbon in intermediate waters off Chile during deglaciation, Nat. Geosci., 3, 192–195, https://doi.org/10.1038/ngeo745, 2010.

Deplazes, G., Lückge, A., Peterson, L. C., Timmermann, A., Hamann, Y., Hughen, K. A., Röhl, U., Laj, C., Cane, M. A., Sigman, D. M., and Haug, G. H.: Links between tropical rainfall and North Atlantic climate during the last glacial period, Nat. Geosci., 6, 213–217, https://doi.org/10.1038/ngeo1712, 2013.

Diaz, H. F. and Markgraf, V.: El Niño: Historical and Paleoclimatic Aspects of the Southern Oscillation, Cambridge University Press, 510 pp., 1992.

Diefendorf, A. F., Leslie, A. B., and Wing, S. L.: Leaf wax composition and carbon isotopes vary among major conifer groups, Geochim. Cosmochim. Acta, 170, 145–156, https://doi.org/10.1016/j.gca.2015.08.018, 2015.

Dima, I. M. and Wallace, J. M.: On the Seasonality of the Hadley Cell, J. Atmospheric Sci., 60, 1522–1527, https://doi.org/10.1175/1520-0469(2003)060<1522:OTSOTH>2.0.CO;2, 2003.

https://doi.org/10.5194/egusphere-2025-3153
Preprint. Discussion started: 10 July 2025

Emile-Geay, J., Cobb, K. M., Carré, M., Braconnot, P., Leloup, J., Zhou, Y., Harrison, S. P., Corrège, T., McGregor, H. V., Collins, M., Driscoll, R., Elliot, M., Schneider, B., and Tudhope, A.: Links between tropical Pacific seasonal, interannual and orbital variability during the Holocene, Nat. Geosci., 9, 168–173, https://doi.org/10.1038/ngeo2608, 2016.

Erb, M. P., McKay, N. P., Steiger, N., Dee, S., Hancock, C., Ivanovic, R. F., Gregoire, L. J., and Valdes, P.: Holocene temperature reconstruction using paleoclimate data assimilation (1.0.0-beta), https://doi.org/10.5281/zenodo.6426332, 2022a.

Erb, M. P., McKay, N. P., Steiger, N., Dee, S., Hancock, C., Ivanovic, R. F., Gregoire, L. J., and Valdes, P.: Reconstructing Holocene temperatures in time and space using paleoclimate data assimilation, Clim. Past, 18, 2599–2629, https://doi.org/10.5194/cp-18-2599-2022, 2022b.

European Commission, Joint Research Centre (JRC): South America Mean Annual Precipitation Map (TRMM 3B43 dataset), 2015.

Fesq-Martin, M., Friedmann, A., Peters, M., Behrmann, J., and Kilian, R.: Late-glacial and Holocene vegetation history of the Magellanic rain forest in southwestern Patagonia, Chile, Veg. Hist. Archaeobotany, 13, 249–255, https://doi.org/10.1007/s00334-004-0047-6, 2004.

Fick, S. E. and Hijmans, R. J.: WorldClim 2: new 1-km spatial resolution climate surfaces for global land areas, Int. J. Climatol., 37, 4302–4315, https://doi.org/10.1002/joc.5086, 2017.

Fiers, G., Bertrand, S., Van Daele, M., Granon, E., Reid, B., Vandoorne, W., and De Batist, M.: Hydroclimate variability of northern Chilean Patagonia during the last 20 kyr inferred from the bulk organic geochemistry of Lago Castor sediments (45°S), Quat. Sci. Rev., 204, 105–118, https://doi.org/10.1016/j.quascirev.2018.11.015, 2019.

Flores-Aqueveque, V., Rojas, M., Aguirre, C., Arias, P. A., and González, C.: South Pacific Subtropical High from the late Holocene to the end of the 21st century: insights from climate proxies and general circulation models, Clim. Past, 16, 79–99, https://doi.org/10.5194/cp-16-79-2020, 2020.

Flores-Aqueveque, V., Ortega, C., Fernández, R., Carabias, D., Simonetti, R., Cartajena, I., Díaz, L., and González, C.: A multi-proxy reconstruction of depositional environment of a Late Pleistocene submerged site from the Central Coast of Chile (32°): Implications for drowned sites, Quat. Int., 601, 15–27, https://doi.org/10.1016/j.quaint.2021.06.005, 2021.

Fogt, R. L. and Bromwich, D. H.: Decadal Variability of the ENSO Teleconnection to the High-Latitude South Pacific Governed by Coupling with the Southern Annular Mode, J. Clim., 19, 979–997, https://doi.org/10.1175/JCLI3671.1, 2006.

Fogt, R. L., Bromwich, D. H., and Hines, K. M.: Understanding the SAM influence on the South Pacific ENSO teleconnection, Clim. Dyn., 36, 1555–1576, https://doi.org/10.1007/s00382-010-0905-0, 2011.

Frugone-Álvarez, M., Latorre, C., Giralt, S., Polanco-Martínez, J., Bernárdez, P., Oliva-Urcia, B., Maldonado, A., Carrevedo, M. L., Moreno, A., Delgado Huertas, A., Prego, R., Barreiro-Lostres, F., and Valero-Garcés, B.: A 7000-year high-resolution lake sediment record from coastal central Chile (Lago Vichuquén, 34°S): implications for past sea level and environmental variability, J. Quat. Sci., 32, 830–844, https://doi.org/10.1002/jqs.2936, 2017.

Gallego, D., Ribera, P., Garcia-Herrera, R., Hernandez, E., and Gimeno, L.: A new look for the Southern Hemisphere jet stream, Clim. Dyn., 24, 607–621, https://doi.org/10.1007/s00382-005-0006-7, 2005.

Garreaud, R. D.: The Andes climate and weather, Adv. Geosci., 22, 3–11, https://doi.org/10.5194/adgeo-22-3-2009, 2009.

Garreaud, R. D. and Battisti, D. S.: Interannual (ENSO) and Interdecadal (ENSO-like) Variability in the Southern Hemisphere Tropospheric Circulation, J. Clim., 12, 2113–2123, https://doi.org/10.1175/1520-0442(1999)012<2113:IEAIEL>2.0.CO;2, 1999.

Garreaud, R. D., Rutllant, J., Quintana, J., Carrasco, J., and Minnis, P.: CIMAR-5: A Snapshot of the Lower Troposphere over the Subtropical Southeast Pacific, Bull. Am. Meteorol. Soc., 82, 2193–2208, https://doi.org/10.1175/1520-0477-82.10.2193, 2001.

Garreaud, R. D., Barichivich, J., Christie, D. A., and Maldonado, A.: Interannual variability of the coastal fog at Fray Jorge relict forests in semiarid Chile, J. Geophys. Res. Biogeosciences, 113, https://doi.org/10.1029/2008JG000709, 2008.

Garreaud, R. D., Vuille, M., Compagnucci, R., and Marengo, J.: Present-day South American climate, Palaeogeogr. Palaeoclimatol. Palaeoecol., 281, 180–195, https://doi.org/10.1016/j.palaeo.2007.10.032, 2009.

Gaviria-Lugo, N., Läuchli, C., Wittmann, H., Bernhard, A., Frings, P., Mohtadi, M., Rach, O., and Sachse, D.: Climatic controls on leaf wax hydrogen isotope ratios in terrestrial and marine sediments along a hyperarid to humid gradient, EGUsphere, 1–34, https://doi.org/10.5194/egusphere-2023-831, 2023a.

Gaviria-Lugo, N., Läuchli, C., Wittmann, H., Bernhard, A., Frings, P., Mohtadi, M., Rach, O., and Sachse, D.: Data of leaf wax hydrogen isotope ratios and climatic variables along an aridity gradient in Chile and globally, https://doi.org/10.5880/GFZ.3.3.2023.001, 2023b.

The GEBCO_2019 Grid - a continuous terrain model of the global oceans and land.:

Geen, R., Bordoni, S., Battisti, D. S., and Hui, K.: Monsoons, ITCZs, and the Concept of the Global Monsoon, Rev. Geophys., 58, e2020RG000700, https://doi.org/10.1029/2020RG000700, 2020.

Gillett, N. P., Kell, T. D., and Jones, P. D.: Regional climate impacts of the Southern Annular Mode, Geophys. Res. Lett., 33, https://doi.org/10.1029/2006GL027721, 2006.

Gong, D. and Wang, S.: Definition of Antarctic Oscillation index, Geophys. Res. Lett., 26, 459–462, https://doi.org/10.1029/1999GL900003, 1999.

Graven, H., Allison, C. E., Etheridge, D. M., Hammer, S., Keeling, R. F., Levin, I., Meijer, H. A. J., Rubino, M., Tans, P. P., Trudinger, C. M., Vaughn, B. H., and White, J. W. C.: Compiled records of carbon isotopes in atmospheric CO_2 for historical simulations in CMIP6, Geosci. Model Dev., 10, 4405–4417, https://doi.org/10.5194/gmd-10-4405-2017, 2017.

Grimm, A. M.: Interannual climate variability in South America: impacts on seasonal precipitation, extreme events, and possible effects of climate change, Stoch. Environ. Res. Risk Assess., 25, 537–554, https://doi.org/10.1007/s00477-010-0420-1, 2011.

Group, G. B. C.: The GEBCO_2019 grid—A continuous terrain model of the global oceans and land, Liverp. UK Br. Oceanogr. Data Cent. Natl. Oceanogr. Cent. NERC, 2019.

Haberle, S. G. and Bennett, K. D.: Postglacial formation and dynamics of North Patagonian Rainforest in the Chonos Archipelago, Southern Chile, Quat. Sci. Rev., 23, 2433–2452, https://doi.org/10.1016/j.quascirev.2004.03.001, 2004.

Haddam, N. A., Siani, G., Michel, E., Kaiser, J., Lamy, F., Duchamp-Alphonse, S., Hefter, J., Braconnot, P., Dewilde, F., Isgüder, G., Tisnerat-Laborde, N., Thil, F., Durand, N., and Kissel, C.: Changes in latitudinal sea surface temperature gradients along the Southern Chilean margin since the last glacial, Quat. Sci. Rev., 194, 62–76, https://doi.org/10.1016/j.quascirev.2018.06.023, 2018.

Hadley, G.: VI. Concerning the cause of the general trade-winds, Philos. Trans. R. Soc. Lond., 39, 58–62, https://doi.org/10.1098/rstl.1735.0014, 1997.

Haug, G. H., Hughen, K. A., Sigman, D. M., Peterson, L. S., and Röhl, U.: Cariaco basin trace metal data (titanium) of ODP Hole 165-1002C, https://doi.org/10.1594/PANGAEA.81965, 2001a.

Haug, G. H., Hughen, K. A., Sigman, D. M., Peterson, L. C., and Röhl, U.: Southward Migration of the Intertropical Convergence Zone Through the Holocene, Science, 293, 1304–1308, https://doi.org/10.1126/science.1059725, 2001b.

Heaton, T. J., Köhler, P., Butzin, M., Bard, E., Reimer, R. W., Austin, W. E. N., Ramsey, C. B., Grootes, P. M., Hughen, K. A., Kromer, B., Reimer, P. J., Adkins, J., Burke, A., Cook, M. S., Olsen, J., and Skinner, L. C.: Marine20—The Marine Radiocarbon Age Calibration Curve (0–55,000 cal BP), Radiocarbon, 62, 779–820, https://doi.org/10.1017/RDC.2020.68, 2020.

Hebbeln, D. and Shipboard Scientists: PUCK: Report and preliminary results of R/V Sonne Cruise SO156, Valparaiso (Chile) - Talcahuano (Chile). March 29 - May 14, 2001, Department of Geosciences, Bremen University, 195 pp., 2001.

Hebbeln, D. and Shipboard Scientists, (last): Cruise report of R/V Sonne Cruise SO-102, Valparaiso (Chile)-Valparaiso (Chile).May 09–June 28, 1995, Berichte Fachbereich Geowiss. Univ. Brem. Brem., 1995.

Held, I. M. and Hou, A. Y.: Nonlinear Axially Symmetric Circulations in a Nearly Inviscid Atmosphere, J. Atmospheric Sci., 37, 515–533, https://doi.org/10.1175/1520-0469(1980)037<0515:NASCIA>2.0.CO;2, 1980.

Heusser, C. J., Heusser, L. E., Lowell, T. V., M., A. M., and M., S. M.: Deglacial palaeoclimate at Puerto del Hambre, subantarctic Patagonia, Chile, J. Quat. Sci., 15, 101–114, https://doi.org/10.1002/(SICI)1099-1417(200002)15:2<101::AID-JQS500>3.0.CO;2-Y, 2000.

Heusser, L. E., Heusser, C. J., Mix, A., and McManus, J.: Chilean and Southeast Pacific paleoclimate variations during the last glacial cycle: directly correlated pollen and δ18O records from ODP Site 1234, Quat. Sci. Rev., 25, 3404–3415, https://doi.org/10.1016/j.quascirev.2006.03.011, 2006a.

Heusser, L. E., Heusser, C. J., and Pisias, N.: Vegetation and climate dynamics of southern Chile during the past 50,000 years: results of ODP Site 1233 pollen analysis, Quat. Sci. Rev., 25, 474–485, https://doi.org/10.1016/j.quascirev.2005.04.009, 2006b.

Hogg, A. G., Heaton, T. J., Hua, Q., Palmer, J. G., Turney, C. S., Southon, J., Bayliss, A., Blackwell, P. G., Boswijk, G., Ramsey, C. B., Pearson, C., Petchey, F., Reimer, P., Reimer, R., and Wacker, L.: SHCal20 Southern Hemisphere Calibration, 0–55,000 Years cal BP, Radiocarbon, 62, 759–778, https://doi.org/10.1017/RDC.2020.59, 2020.

Inatsu, M. and Hoskins, B. J.: The Zonal Asymmetry of the Southern Hemisphere Winter Storm Track, J. Clim., 17, 4882–4892, https://doi.org/10.1175/JCLI-3232.1, 2004.

Jara, I. A. and Moreno, P. I.: Temperate rainforest response to climate change and disturbance agents in northwestern Patagonia (41°S) over the last 2600 years, Quat. Res., 77, 235–244, https://doi.org/10.1016/j.yqres.2011.11.011, 2012.

Jara, I. A. and Moreno, P. I.: Climatic and disturbance influences on the temperate rainforests of northwestern Patagonia (40 °S) since ~14,500 cal yr BP, Quat. Sci. Rev., 90, 217–228, https://doi.org/10.1016/j.quascirev.2014.01.024, 2014.

Jenny, B., Valero-Garcés, B. L., Villa-Martínez, R., Urrutia, R., Geyh, M., and Veit, H.: Early to Mid-Holocene Aridity in Central Chile and the Southern Westerlies: The Laguna Aculeo Record (34°S), Quat. Res., 58, 160–170, https://doi.org/10.1006/qres.2002.2370, 2002a.

Jenny, B., Valero-Garcés, B. L., Urrutia, R., Kelts, K., Veit, H., Appleby, P. G., and Geyh, M.: Moisture changes and fluctuations of the Westerlies in Mediterranean Central Chile during the last 2000 years: The Laguna Aculeo record (33°50′S), Quat. Int., 87, 3–18, https://doi.org/10.1016/S1040-6182(01)00058-1, 2002b.

Jenny, B., Wilhelm, D., and Valero-Garcés, B.: The Southern Westerlies in Central Chile: Holocene precipitation estimates based on a water balance model for Laguna Aculeo (33°50′S), Clim. Dyn., 20, 269–280, https://doi.org/10.1007/s00382-002-0267-3, 2003.

Joshi, M. M., Gregory, J. M., Webb, M. J., Sexton, D. M. H., and Johns, T. C.: Mechanisms for the land/sea warming contrast exhibited by simulations of climate change, Clim. Dyn., 30, 455–465, https://doi.org/10.1007/s00382-007-0306-1, 2008.

Kahmen, A., Schefuß, E., and Sachse, D.: Leaf water deuterium enrichment shapes leaf wax *n*-alkane δD values of angiosperm plants I: Experimental evidence and mechanistic insights, Geochim. Cosmochim. Acta, 111, 39–49, https://doi.org/10.1016/j.gca.2012.09.003, 2013a.

Kahmen, A., Hoffmann, B., Schefuß, E., Arndt, S. K., Cernusak, L. A., West, J. B., and Sachse, D.: Leaf water deuterium enrichment shapes leaf wax *n*-alkane δD values of angiosperm plants II: Observational evidence and global implications, Geochim. Cosmochim. Acta, 111, 50–63, https://doi.org/10.1016/j.gca.2012.09.004, 2013b.

Kaiser, J., Schefuß, E., Lamy, F., Mohtadi, M., and Hebbeln, D.: Glacial to Holocene changes in sea surface temperature and coastal vegetation in north central Chile: high versus low latitude forcing, Quat. Sci. Rev., 27, 2064–2075, https://doi.org/10.1016/j.quascirev.2008.08.025, 2008.

Kaiser, J., Schefuß, E., Collins, J., Garreaud, R., Stuut, J.-B. W., Ruggieri, N., De Pol-Holz, R., and Lamy, F.: Orbital modulation of subtropical versus subantarctic moisture sources in the southeast Pacific mid-latitudes, Nat. Commun., 15, 7512, https://doi.org/10.1038/s41467-024-51985-4, 2024.

Kim, B.-M., Choi, H., Kim, S.-J., and Choi, W.: Amplitude-dependent relationship between the Southern Annular Mode and the El Niño Southern Oscillation in austral summer, Asia-Pac. J. Atmospheric Sci., 53, 85–100, https://doi.org/10.1007/s13143-017-0007-6, 2017.

Köhler, P., Nehrbass-Ahles, C., Schmitt, J., Stocker, T. F., and Fischer, H.: A 156 kyr smoothed history of the atmospheric greenhouse gases CO_2, CH_4, and N_2O and their radiative forcing, Earth Syst. Sci. Data, 9, 363–387, https://doi.org/10.5194/essd-9-363-2017, 2017a.

Köhler, P., Nehrbass-Ahles, C., Schmitt, J., Stocker, T. F., and Fischer, H.: Continuous record of the atmospheric greenhouse gas carbon dioxide (CO2), final spline-smoothed data of calculated radiative forcing (Version 2), https://doi.org/10.1594/PANGAEA.876013, 2017b.

Koutavas, A. and Joanides, S.: El Niño–Southern Oscillation extrema in the Holocene and Last Glacial Maximum, Paleoceanography, 27, https://doi.org/10.1029/2012PA002378, 2012.

Koutavas, A. and Lynch-Stieglitz, J.: Variability of the Marine ITCZ over the Eastern Pacific during the Past 30,000 Years, in: The Hadley Circulation: Present, Past and Future, edited by: Diaz, H. F. and Bradley, R. S., Springer Netherlands, Dordrecht, 347–369, https://doi.org/10.1007/978-1-4020-2944-8_13, 2004.

Koutavas, A., Lynch-Stieglitz, J., Marchitto, T. M., and Sachs, J. P.: El Niño-Like Pattern in Ice Age Tropical Pacific Sea Surface Temperature, Science, 297, 226–230, https://doi.org/10.1126/science.1072376, 2002.

Koutavas, A., deMenocal, P. B., Olive, G. C., and Lynch-Stieglitz, J.: Mid-Holocene El Niño–Southern Oscillation (ENSO) attenuation revealed by individual foraminifera in eastern tropical Pacific sediments, Geology, 34, 993–996, https://doi.org/10.1130/G22810A.1, 2006.

Lamy, F., Hebbeln, D., and Wefer, G.: Terrigenous sediment supply along the Chilean continental margin: modern regional patterns of texture and composition, Geol. Rundsch., 87, 477–494, https://doi.org/10.1007/s005310050223, 1998.

Lamy, F., Hebbeln, D., and Wefer, G.: High-Resolution Marine Record of Climatic Change in Mid-latitude Chile during the Last 28,000 Years Based on Terrigenous Sediment Parameters, Quat. Res., 51, 83–93, https://doi.org/10.1006/qres.1998.2010, 1999.

Lamy, F., Hebbeln, D., Röhl, U., and Wefer, G.: Holocene rainfall variability in southern Chile: a marine record of latitudinal shifts of the Southern Westerlies, Earth Planet. Sci. Lett., 185, 369–382, https://doi.org/10.1016/S0012-821X(00)00381-2, 2001.

Lamy, F., Kilian, R., Arz, H. W., Francois, J.-P., Kaiser, J., Prange, M., and Steinke, T.: Holocene changes in the position and intensity of the southern westerly wind belt, Nat. Geosci., 3, 695–699, https://doi.org/10.1038/ngeo959, 2010.

Lamy, F., Chiang, J. C. H., Martínez-Méndez, G., Thierens, M., Arz, H. W., Bosmans, J., Hebbeln, D., Lambert, F., Lembke-Jene, L., and Stuut, J.-B.: Precession modulation of the South Pacific westerly wind belt over the past million years, Proc. Natl. Acad. Sci., 116, 23455–23460, https://doi.org/10.1073/pnas.1905847116, 2019.

Läuchli, C., Gaviria-Lugo, N., Bernhardt, A., Wittmann, H., Frings, P., Mohtadi, M., Lückge, A., and Sachse, D.: Carbon and hydrogen isotope compositions of leaf wax n-alkanes, climate variables and age-depth models used to constrain hydrological regimes along Chile during the last 20,000 years., 2025.

Lee, S.-Y., Chiang, J. C. H., Matsumoto, K., and Tokos, K. S.: Southern Ocean wind response to North Atlantic cooling and the rise in atmospheric CO2: Modeling perspective and paleoceanographic implications, Paleoceanography, 26, https://doi.org/10.1029/2010PA002004, 2011.

Lehner, B. and Grill, G.: Global river hydrography and network routing: baseline data and new approaches to study the world's large river systems, Hydrol. Process., 27, 2171–2186, https://doi.org/10.1002/hyp.9740, 2013.

Lehner, B., Verdin, K., and Jarvis, A.: HydroSHEDS technical documentation, World Wildl. Fund US Wash. DC, 5, 2006.

Li, Y., Xie, S.-P., Lian, T., Zhang, G., Feng, J., Ma, J., Peng, Q., Wang, W., Hou, Y., and Li, X.: Interannual Variability of Regional Hadley Circulation and El Niño Interaction, Geophys. Res. Lett., 50, e2022GL102016, https://doi.org/10.1029/2022GL102016, 2023.

Lindzen, R. S. and Hou, A. V.: Hadley Circulations for Zonally Averaged Heating Centered off the Equator, J. Atmospheric Sci., 45, 2416–2427, https://doi.org/10.1175/1520-0469(1988)045<2416:HCFZAH>2.0.CO;2, 1988.

Lippold, J., Pöppelmeier, F., Süfke, F., Gutjahr, M., Goepfert, T. J., Blaser, P., Friedrich, O., Link, J. M., Wacker, L., Rheinberger, S., and Jaccard, S. L.: Constraining the Variability of the Atlantic Meridional Overturning Circulation During the Holocene, Geophys. Res. Lett., 46, 11338–11346, https://doi.org/10.1029/2019GL084988, 2019.

Liu, W. and Yang, H.: Multiple controls for the variability of hydrogen isotopic compositions in higher plant n-alkanes from modern ecosystems, Glob. Change Biol., 14, 2166–2177, https://doi.org/10.1111/j.1365-2486.2008.01608.x, 2008.

Liu, W., Yang, H., Wang, H., An, Z., Wang, Z., and Leng, Q.: Carbon isotope composition of long chain leaf wax *n*-alkanes in lake sediments: A dual indicator of paleoenvironment in the Qinghai-Tibet Plateau, Org. Geochem., 83–84, 190–201, https://doi.org/10.1016/j.orggeochem.2015.03.017, 2015.

Lowrie, A. and Hey, R.: Geological and geophysical variations along the western margin of Chile near lat 33° to 36° S and their relation to Nazca plate subduction, in: Nazca Plate: Crustal Formation and Andean Convergence, edited by: Kulm, L. V. D., Dymond, J., Dasch, E. J., Hussong, D. M., and Roderick, R., Geological Society of America, 0, https://doi.org/10.1130/MEM154-p741, 1981.

Luebert, F.: The two South American dry diagonals, Front. Biogeogr., 13, https://doi.org/10.21425/F5FBG51267, 2021.

Madden, R. A. and Julian, P. R.: Observations of the 40–50-Day Tropical Oscillation—A Review, Mon. Weather Rev., 122, 814–837, https://doi.org/10.1175/1520-0493(1994)122<0814:OOTDTO>2.0.CO;2, 1994.

Maldonado, A. and Villagrán, C.: Paleoenvironmental Changes in the Semiarid Coast of Chile (~32°S) during the Last 6200 cal Years Inferred from a Swamp–Forest Pollen Record, Quat. Res., 58, 130–138, https://doi.org/10.1006/qres.2002.2353, 2002.

Maldonado, A. and Villagrán, C.: Climate variability over the last 9900 cal yr BP from a swamp forest pollen record along the semiarid coast of Chile, Quat. Res., 66, 246–258, https://doi.org/10.1016/j.yqres.2006.04.003, 2006.

Maldonado, A., Méndez, C., Ugalde, P., Jackson, D., Seguel, R., and Latorre, C.: Early Holocene climate change and human occupation along the semiarid coast of north-central Chile, J. Quat. Sci., 25, 985–988, https://doi.org/10.1002/jqs.1385, 2010.

Marshall, G. J.: Trends in the Southern Annular Mode from Observations and Reanalyses, J. Clim., 16, 4134–4143, https://doi.org/10.1175/1520-0442(2003)016<4134:TITSAM>2.0.CO;2, 2003.

Martínez Fontaine, C., De Pol-Holz, R., Michel, E., Siani, G., Reyes-Macaya, D., Martínez-Méndez, G., DeVries, T., Stott, L., Southon, J., Mohtadi, M., and Hebbeln, D.: Ventilation of the Deep Ocean Carbon Reservoir During the Last Deglaciation: Results From the Southeast Pacific, Paleoceanogr. Paleoclimatology, 34, 2080–2097, https://doi.org/10.1029/2019PA003613, 2019.

McManus, J. F., Francois, R., Gherardi, J.-M., Keigwin, L. D., and Brown-Leger, S.: Collapse and rapid resumption of Atlantic meridional circulation linked to deglacial climate changes, Nature, 428, 834–837, https://doi.org/10.1038/nature02494, 2004.

Menviel, L., Spence, P., Yu, J., Chamberlain, M. A., Matear, R. J., Meissner, K. J., and England, M. H.: Southern Hemisphere westerlies as a driver of the early deglacial atmospheric CO2 rise, Nat. Commun., 9, 2503, https://doi.org/10.1038/s41467-018-04876-4, 2018.

Merino-Campos, V., Pol-Holz, R. D., Southon, J., Latorre, C., and Collado-Fabbri, S.: Marine Radiocarbon Reservoir Age Along the Chilean Continental Margin, Radiocarbon, 61, 195–210, https://doi.org/10.1017/RDC.2018.81, 2019.

Mo, K. C. and Paegle, J. N.: The Pacific–South American modes and their downstream effects, Int. J. Climatol., 21, 1211–1229, https://doi.org/10.1002/joc.685, 2001.

Mohtadi, M. and Hebbeln, D.: Mechanisms and variations of the paleoproductivity off northern Chile (24°S–33°S) during the last 40,000 years, Paleoceanography, 19, https://doi.org/10.1029/2004PA001003, 2004.

Mohtadi, M., Prange, M., and Steinke, S.: Palaeoclimatic insights into forcing and response of monsoon rainfall, Nature, 533, 191–199, https://doi.org/10.1038/nature17450, 2016.

Monnin, E.: EPICA Dome C high resolution carbon dioxide concentrations, https://doi.org/10.1594/PANGAEA.472488, 2006.

Montade, V., Combourieu Nebout, N., Kissel, C., Haberle, S. G., Siani, G., and Michel, E.: Vegetation and climate changes during the last 22,000yr from a marine core near Taitao Peninsula, southern Chile, Palaeogeogr. Palaeoclimatol. Palaeoecol., 369, 335–348, https://doi.org/10.1016/j.palaeo.2012.11.001, 2013.

Montecinos, A. and Aceituno, P.: Seasonality of the ENSO-Related Rainfall Variability in Central Chile and Associated Circulation Anomalies, J. Clim., 16, 281–296, https://doi.org/10.1175/1520-0442(2003)016<0281:SOTERR>2.0.CO;2, 2003.

Montecinos, A., Díaz, A., and Aceituno, P.: Seasonal Diagnostic and Predictability of Rainfall in Subtropical South America Based on Tropical Pacific SST, J. Clim., 13, 746–758, https://doi.org/10.1175/1520-0442(2000)013<0746:SDAPOR>2.0.CO;2, 2000.

Moreno, P. I.: Millennial-scale climate variability in northwest Patagonia over the last 15 000 yr, J. Quat. Sci., 19, 35–47, https://doi.org/10.1002/jqs.813, 2004.

Moreno, P. I. and León, A. L.: Abrupt vegetation changes during the last glacial to Holocene transition in mid-latitude South America, J. Quat. Sci., 18, 787–800, https://doi.org/10.1002/jqs.801, 2003.

Moreno, P. I. and Videla, J.: Centennial and millennial-scale hydroclimate changes in northwestern Patagonia since 16,000 yr BP, Quat. Sci. Rev., 149, 326–337, https://doi.org/10.1016/j.quascirev.2016.08.008, 2016.

Moreno, P. I., Francois, J. P., Moy, C. M., and Villa-Martínez, R.: Covariability of the Southern Westerlies and atmospheric CO2 during the Holocene, Geology, 38, 727–730, https://doi.org/10.1130/G30962.1, 2010.

Moreno, P. I., Videla, J., Valero-Garcés, B., Alloway, B. V., and Heusser, L. E.: A continuous record of vegetation, fire-regime and climatic changes in northwestern Patagonia spanning the last 25,000 years, Quat. Sci. Rev., 198, 15–36, https://doi.org/10.1016/j.quascirev.2018.08.013, 2018.

Moreno, P. I., Henríquez, W. I., Pesce, O. H., Henríquez, C. A., Fletcher, M. S., Garreaud, R. D., and Villa-Martínez, R. P.: An early Holocene westerly minimum in the southern mid-latitudes, Quat. Sci. Rev., 251, 106730, https://doi.org/10.1016/j.quascirev.2020.106730, 2021.

Moreno-Chamarro, E., Marshall, J., and Delworth, T. L.: Linking ITCZ Migrations to the AMOC and North Atlantic/Pacific SST Decadal Variability, https://doi.org/10.1175/JCLI-D-19-0258.1, 2019.

Muñoz, P., Rebolledo, L., Dezileau, L., Maldonado, A., Mayr, C., Cárdenas, P., Lange, C. B., Lalangui, K., Sanchez, G., Salamanca, M., Araya, K., Jara, I., Easton, G., and Ramos, M.: Reconstructing past variations in environmental conditions and paleoproductivity over the last ∼ 8000 years off north-central Chile (30° S), Biogeosciences, 17, 5763–5785, https://doi.org/10.5194/bg-17-5763-2020, 2020.

Muratli, J. M., Chase, Z., McManus, J., and Mix, A.: Ice-sheet control of continental erosion in central and southern Chile (36°–41°S) over the last 30,000 years, Quat. Sci. Rev., 29, 3230–3239, https://doi.org/10.1016/j.quascirev.2010.06.037, 2010.

Nakamura, H. and Shimpo, A.: Seasonal Variations in the Southern Hemisphere Storm Tracks and Jet Streams as Revealed in a Reanalysis Dataset, J. Clim., 17, 1828–1844, https://doi.org/10.1175/1520-0442(2004)017<1828:SVITSH>2.0.CO;2, 2004.

Nakamura, H., Sampe, T., Tanimoto, Y., and Shimpo, A.: Observed Associations Among Storm Tracks, Jet Streams and Midlatitude Oceanic Fronts, in: Earth's Climate, American Geophysical Union (AGU), 329–345, https://doi.org/10.1029/147GM18, 2004.

Nguyen, H., Evans, A., Lucas, C., Smith, I., and Timbal, B.: The Hadley Circulation in Reanalyses: Climatology, Variability, and Change, J. Clim., 26, 3357–3376, https://doi.org/10.1175/JCLI-D-12-00224.1, 2013.

Niedermeyer, E. M., Forrest, M., Beckmann, B., Sessions, A. L., Mulch, A., and Schefuß, E.: The stable hydrogen isotopic composition of sedimentary plant waxes as quantitative proxy for rainfall in the West African Sahel, Geochim. Cosmochim. Acta, 184, 55–70, https://doi.org/10.1016/j.gca.2016.03.034, 2016.

Oort, A. H. and Yienger, J. J.: Observed Interannual Variability in the Hadley Circulation and Its Connection to ENSO, J. Clim., 9, 2751–2767, https://doi.org/10.1175/1520-0442(1996)009<2751:OIVITH>2.0.CO;2, 1996.

Ortega, C., Vargas, G., Rutllant, J. A., Jackson, D., and Méndez, C.: Major hydrological regime change along the semiarid western coast of South America during the early Holocene, Quat. Res., 78, 513–527, https://doi.org/10.1016/j.yqres.2012.08.002, 2012.

Ortega, C., Vargas, G., Rojas, M., Rutllant, J. A., Muñoz, P., Lange, C. B., Pantoja, S., Dezileau, L., and Ortlieb, L.: Extreme ENSO-driven torrential rainfalls at the southern edge of the Atacama Desert during the Late Holocene and their projection into the 21th century, Glob. Planet. Change, 175, 226–237, https://doi.org/10.1016/j.gloplacha.2019.02.011, 2019.

Osman, M. B., Tierney, J. E., Zhu, J., Tardif, R., Hakim, G. J., King, J., and Poulsen, C. J.: Globally resolved surface temperatures since the Last Glacial Maximum, Nature, 599, 239–244, https://doi.org/10.1038/s41586-021-03984-4, 2021.

Pedro, J. B., Bostock, H. C., Bitz, C. M., He, F., Vandergoes, M. J., Steig, E. J., Chase, B. M., Krause, C. E., Rasmussen, S. O., Markle, B. R., and Cortese, G.: The spatial extent and dynamics of the Antarctic Cold Reversal, Nat. Geosci., 9, 51–55, https://doi.org/10.1038/ngeo2580, 2016.

Pedro, J. B., Jochum, M., Buizert, C., He, F., Barker, S., and Rasmussen, S. O.: Beyond the bipolar seesaw: Toward a process understanding of interhemispheric coupling, Quat. Sci. Rev., 192, 27–46, https://doi.org/10.1016/j.quascirev.2018.05.005, 2018.

Perren, B. B., Kaiser, J., Arz, H. W., Dellwig, O., Hodgson, D. A., and Lamy, F.: Poleward displacement of the Southern Hemisphere Westerlies in response to Early Holocene warming, Commun. Earth Environ., 6, 1–10, https://doi.org/10.1038/s43247-025-02129-z, 2025.

Pesce, O. H. and Moreno, P. I.: Vegetation, fire and climate change in central-east Isla Grande de Chiloé (43°S) since the Last Glacial Maximum, northwestern Patagonia, Quat. Sci. Rev., 90, 143–157, https://doi.org/10.1016/j.quascirev.2014.02.021, 2014.

Pezza, A. B., Simmonds, I., and Renwick, J. A.: Southern hemisphere cyclones and anticyclones: recent trends and links with decadal variability in the Pacific Ocean, Int. J. Climatol., 27, 1403–1419, https://doi.org/10.1002/joc.1477, 2007.

Polissar, P. J., Freeman, K. H., Rowley, D. B., McInerney, F. A., and Currie, B. S.: Paleoaltimetry of the Tibetan Plateau from D/H ratios of lipid biomarkers, Earth Planet. Sci. Lett., 287, 64–76, https://doi.org/10.1016/j.epsl.2009.07.037, 2009.

Pöppelmeier, F., Jeltsch-Thömmes, A., Lippold, J., Joos, F., and Stocker, T. F.: Multi-proxy agreement on Atlantic circulation dynamics since the last ice age: Model output data, https://doi.org/10.5281/zenodo.7540200, 2023a.

Pöppelmeier, F., Jeltsch-Thömmes, A., Lippold, J., Joos, F., and Stocker, T. F.: Multi-proxy constraints on Atlantic circulation dynamics since the last ice age, Nat. Geosci., 16, 349–356, https://doi.org/10.1038/s41561-023-01140-3, 2023b.

de Porras, M. E., Maldonado, A., Quintana, F. A., Martel-Cea, A., Reyes, O., and Méndez, C.: Environmental and climatic changes in central Chilean Patagonia since the Late Glacial (Mallín El Embudo, 44° S), Clim. Past, 10, 1063–1078, https://doi.org/10.5194/cp-10-1063-2014, 2014.

Powell, R. L. and Still, C. J.: Biogeography of C3 and C4 vegetation in South America, Simpósio Brasileiro de Sensoriamento Remoto, 14 (SBSR), 2935–2942, 2009.

Prohaska, A., Seddon, A. W. R., Meese, B., Willis, K. J., Chiang, J. C. H., and Sachse, D.: Abrupt change in tropical Pacific climate mean state during the Little Ice Age, Commun. Earth Environ., 4, 1–13, https://doi.org/10.1038/s43247-023-00882-7, 2023.

Putman, A. L., Feng, X., Sonder, L. J., and Posmentier, E. S.: Annual variation in event-scale precipitation δ^2H at Barrow, AK, reflects vapor source region, Atmospheric Chem. Phys., 17, 4627–4639, https://doi.org/10.5194/acp-17-4627-2017, 2017.

Quade, J. and Kaplan, M. R.: Lake-level stratigraphy and geochronology revisited at Lago (Lake) Cardiel, Argentina, and changes in the Southern Hemispheric Westerlies over the last 25 ka, Quat. Sci. Rev., 177, 173–188, https://doi.org/10.1016/j.quascirev.2017.10.006, 2017.

Rach, O., Brauer, A., Wilkes, H., and Sachse, D.: Delayed hydrological response to Greenland cooling at the onset of the Younger Dryas in western Europe, Nat. Geosci., 7, 109–112, https://doi.org/10.1038/ngeo2053, 2014.

Rach, O., Hadeen, X., and Sachse, D.: An automated solid phase extraction procedure for lipid biomarker purification and stable isotope analysis, Org. Geochem., 142, 103995, https://doi.org/10.1016/j.orggeochem.2020.103995, 2020.

Rahn, D. A. and Garreaud, R. D.: A synoptic climatology of the near-surface wind along the west coast of South America, Int. J. Climatol., 34, 780–792, https://doi.org/10.1002/joc.3724, 2014.

Reboita, M. S., Ambrizzi, T., Crespo, N. M., Dutra, L. M. M., Ferreira, G. W. de S., Rehbein, A., Drumond, A., da Rocha, R. P., and Souza, C. A. de: Impacts of teleconnection patterns on South America climate, Ann. N. Y. Acad. Sci., 1504, 116–153, https://doi.org/10.1111/nyas.14592, 2021.

Reimi, M. A. and Marcantonio, F.: Constraints on the magnitude of the deglacial migration of the ITCZ in the Central Equatorial Pacific Ocean, Earth Planet. Sci. Lett., 453, 1–8, https://doi.org/10.1016/j.epsl.2016.07.058, 2016.

Renssen, H., Goosse, H., Fichefet, T., and Campin, J.-M.: The 8.2 kyr BP event simulated by a Global Atmosphere—Sea-Ice—Ocean Model, Geophys. Res. Lett., 28, 1567–1570, https://doi.org/10.1029/2000GL012602, 2001.

Rozanski, K., Araguás-Araguás, L., and Gonfiantini, R.: Isotopic Patterns in Modern Global Precipitation, in: Climate Change in Continental Isotopic Records, American Geophysical Union (AGU), 1–36, https://doi.org/10.1029/GM078p0001, 1993.

Rutllant, J. and Fuenzalida, H.: Synoptic aspects of the central chile rainfall variability associated with the southern oscillation, Int. J. Climatol., 11, 63–76, https://doi.org/10.1002/joc.3370110105, 1991.

Sachs, J. P., Sachse, D., Smittenberg, R. H., Zhang, Z., Battisti, D. S., and Golubic, S.: Southward movement of the Pacific intertropical convergence zone AD 1400–1850, Nat. Geosci., 2, 519–525, https://doi.org/10.1038/ngeo554, 2009.

Sachse, D., Radke, J., and Gleixner, G.: Hydrogen isotope ratios of recent lacustrine sedimentary n-alkanes record modern climate variability, Geochim. Cosmochim. Acta, 68, 4877–4889, https://doi.org/10.1016/j.gca.2004.06.004, 2004.

Sachse, D., Radke, J., and Gleixner, G.: δD values of individual n-alkanes from terrestrial plants along a climatic gradient – Implications for the sedimentary biomarker record, Org. Geochem., 37, 469–483, https://doi.org/10.1016/j.orggeochem.2005.12.003, 2006.

Sachse, D., Billault, I., Bowen, G. J., Chikaraishi, Y., Dawson, T. E., Feakins, S. J., Freeman, K. H., Magill, C. R., McInerney, F. A., van der Meer, M. T. J., Polissar, P., Robins, R. J., Sachs, J. P., Schmidt, H.-L., Sessions, A. L., White, J. W. C., West, J. B., and Kahmen, A.: Molecular Paleohydrology: Interpreting the Hydrogen-Isotopic Composition of Lipid Biomarkers from Photosynthesizing Organisms, Annu. Rev. Earth Planet. Sci., 40, 221–249, https://doi.org/10.1146/annurev-earth-042711-105535, 2012.

Salati, E., Dall'Olio, A., Matsui, E., and Gat, J. R.: Recycling of water in the Amazon Basin: An isotopic study, Water Resour. Res., 15, 1250–1258, https://doi.org/10.1029/WR015i005p01250, 1979.

Salvatteci, R., Schneider, R. R., Blanz, T., and Mollier-Vogel, E.: Deglacial to Holocene Ocean Temperatures in the Humboldt Current System as Indicated by Alkenone Paleothermometry, Geophys. Res. Lett., 46, 281–292, https://doi.org/10.1029/2018GL080634, 2019.

Sandweiss, D. H., Richardson, J. B., Reitz, E. J., Rollins, H. B., and Maasch, K. A.: Geoarchaeological Evidence from Peru for a 5000 Years B.P. Onset of El Niño, Science, 273, 1531–1533, https://doi.org/10.1126/science.273.5281.1531, 1996.

Schefuß, E., Schouten, S., and Schneider, R. R.: Climatic controls on central African hydrology during the past 20,000 years, Nature, 437, 1003–1006, https://doi.org/10.1038/nature03945, 2005.

Schneider, T., Bischoff, T., and Haug, G. H.: Migrations and dynamics of the intertropical convergence zone, Nature, 513, 45–53, https://doi.org/10.1038/nature13636, 2014.

Schneider, W., Donoso, D., Garcés-Vargas, J., and Escribano, R.: Water-column cooling and sea surface salinity increase in the upwelling region off central-south Chile driven by a poleward displacement of the South Pacific High, Prog. Oceanogr., 151, 38–48, https://doi.org/10.1016/j.pocean.2016.11.004, 2017.

Sessions, A. L., Burgoyne, T. W., Schimmelmann, A., and Hayes, J. M.: Fractionation of hydrogen isotopes in lipid biosynthesis, Org. Geochem., 30, 1193–1200, https://doi.org/10.1016/S0146-6380(99)00094-7, 1999.

Shakun, J. D., Clark, P. U., He, F., Marcott, S. A., Mix, A. C., Liu, Z., Otto-Bliesner, B., Schmittner, A., and Bard, E.: Global warming preceded by increasing carbon dioxide concentrations during the last deglaciation, Nature, 484, 49–54, https://doi.org/10.1038/nature10915, 2012.

Shi, X., Werner, M., Yang, H., D'Agostino, R., Liu, J., Yang, C., and Lohmann, G.: Unraveling the complexities of the Last Glacial Maximum climate: the role of individual boundary conditions and forcings, Clim. Past, 19, 2157–2175, https://doi.org/10.5194/cp-19-2157-2023, 2023.

Siani, G., Michel, E., De Pol-Holz, R., DeVries, T., Lamy, F., Carel, M., Isguder, G., Dewilde, F., and Lourantou, A.: Carbon isotope records reveal precise timing of enhanced Southern Ocean upwelling during the last deglaciation, Nat. Commun., 4, 2758, https://doi.org/10.1038/ncomms3758, 2013.

Silva, N., Rojas, N., and Fedele, A.: Water masses in the Humboldt Current System: Properties, distribution, and the nitrate deficit as a chemical water mass tracer for Equatorial Subsurface Water off Chile, Deep Sea Res. Part II Top. Stud. Oceanogr., 56, 1004–1020, https://doi.org/10.1016/j.dsr2.2008.12.013, 2009.

Sinclair, M. R., Renwick, J. A., and Kidson, J. W.: Low-Frequency Variability of Southern Hemisphere Sea Level Pressure and Weather System Activity, Mon. Weather Rev., 125, 2531–2543, https://doi.org/10.1175/1520-0493(1997)125<2531:LFVOSH>2.0.CO;2, 1997.

Strub, P. T., Mesías, J., Montecino, V., Rutllant, J. A., and Salinas, S.: Coastal ocean circulation off Western South America, Robinson, A. R., and K. H. Brink, Eds., John Wiley and Sons, NY, 273-313. pp., 1998.

Stuut, J.-B. W. and Lamy, F.: Climate variability at the southern boundaries of the Namib (southwestern Africa) and Atacama (northern Chile) coastal deserts during the last 120,000 yr, Quat. Res., 62, 301–309, https://doi.org/10.1016/j.yqres.2004.08.001, 2004.

Stuut, J.-B. W., Kasten, S., Lamy, F., and Hebbeln, D.: Sources and modes of terrigenous sediment input to the Chilean continental slope, Quat. Int., 161, 67–76, https://doi.org/10.1016/j.quaint.2006.10.041, 2007.

Thomas, E. R., Wolff, E. W., Mulvaney, R., Steffensen, J. P., Johnsen, S. J., Arrowsmith, C., White, J. W. C., Vaughn, B., and Popp, T.: The 8.2 ka event from Greenland ice cores, Quat. Sci. Rev., 26, 70–81, https://doi.org/10.1016/j.quascirev.2006.07.017, 2007.

Thompson, D. W. J. and Wallace, J. M.: Annular Modes in the Extratropical Circulation. Part I: Month-to-Month Variability, J. Clim., 13, 1000–1016, https://doi.org/10.1175/1520-0442(2000)013<1000:AMITEC>2.0.CO;2, 2000.

Tian, L., Yao, T., MacClune, K., White, J. W. C., Schilla, A., Vaughn, B., Vachon, R., and Ichiyanagi, K.: Stable isotopic variations in west China: A consideration of moisture sources, J. Geophys. Res. Atmospheres, 112, https://doi.org/10.1029/2006JD007718, 2007.

Tiner, R. J., Negrini, R. M., Antinao, J. L., McDonald, E., and Maldonado, A.: Geophysical and geochemical constraints on the age and paleoclimate implications of Holocene lacustrine cores from the Andes of central Chile, J. Quat. Sci., 33, 150–165, https://doi.org/10.1002/jqs.3012, 2018.

Tofelde, S., Bernhardt, A., Guerit, L., and Romans, B. W.: Times Associated With Source-to-Sink Propagation of Environmental Signals During Landscape Transience, Front. Earth Sci., 9, 2021.

Toggweiler, J. R., Russell, J. L., and Carson, S. R.: Midlatitude westerlies, atmospheric CO2, and climate change during the ice ages, Paleoceanography, 21, https://doi.org/10.1029/2005PA001154, 2006.

Turner, J.: The El Niño–southern oscillation and Antarctica, Int. J. Climatol., 24, 1–31, https://doi.org/10.1002/joc.965, 2004.

Umling, N. E. and Thunell, R. C.: Synchronous deglacial thermocline and deep-water ventilation in the eastern equatorial Pacific, Nat. Commun., 8, 14203, https://doi.org/10.1038/ncomms14203, 2017.

Valero-Garcés, B. L., Jenny, B., Rondanelli, M., Delgado-Huertas, A., Burns, S. J., Veit, H., and Moreno, A.: Palaeohydrology of Laguna de Tagua Tagua (34° 30′ S) and moisture fluctuations in Central Chile for the last 46 000 yr, J. Quat. Sci., 20, 625–641, https://doi.org/10.1002/jqs.988, 2005.

Vargas, G., Rutllant, J., and Ortlieb, L.: ENSO tropical–extratropical climate teleconnections and mechanisms for Holocene debris flows along the hyperarid coast of western South America (17°–24°S), Earth Planet. Sci. Lett., 249, 467–483, https://doi.org/10.1016/j.epsl.2006.07.022, 2006.

Vargas-Ramirez, L., Roche, E., Gerrienne, P., and Hooghiemstra, H.: A pollen-based record of late glacial–Holocene climatic variability in the southern lake district, Chile, J. Paleolimnol., 39, 197–217, https://doi.org/10.1007/s10933-007-9115-0, 2008.

Veit, H.: Southern Westerlies during the Holocene deduced from geomorphological and pedological studies in the Norte Chico, Northern Chile (27–33°S), Palaeogeogr. Palaeoclimatol. Palaeoecol., 123, 107–119, https://doi.org/10.1016/0031-0182(95)00118-2, 1996.

Vera, C., Higgins, W., Amador, J., Ambrizzi, T., Garreaud, R., Gochis, D., Gutzler, D., Lettenmaier, D., Marengo, J., Mechoso, C. R., Nogues-Paegle, J., Dias, P. L. S., and Zhang, C.: Toward a Unified View of the American Monsoon Systems, J. Clim., 19, 4977–5000, https://doi.org/10.1175/JCLI3896.1, 2006.

Villa-Martínez, R., Villagrán, C., and Jenny, B.: The last 7500 cal yr B.P. of westerly rainfall in Central Chile inferred from a high-resolution pollen record from Laguna Aculeo (34°S), Quat. Res., 60, 284–293, https://doi.org/10.1016/j.yqres.2003.07.007, 2003.

Villa-Martínez, R., Villagrán, C., and Jenny, B.: Pollen evidence for late-Holocene climatic variability at Laguna de Aculeo, Central Chile (lat. 34°S), The Holocene, 14, 361–367, https://doi.org/10.1191/0959683604hl712rp, 2004.

Völker, C. and Köhler, P.: Responses of ocean circulation and carbon cycle to changes in the position of the Southern Hemisphere westerlies at Last Glacial Maximum, Paleoceanography, 28, 726–739, https://doi.org/10.1002/2013PA002556, 2013.

Waliser, D. E. and Gautier, C.: A Satellite-derived Climatology of the ITCZ, J. Clim., 6, 2162–2174, https://doi.org/10.1175/1520-0442(1993)006<2162:ASDCOT>2.0.CO;2, 1993.

Waterisotopes Database: Global precipitation, 2017.

Watt-Meyer, O. and Frierson, D. M. W.: ITCZ Width Controls on Hadley Cell Extent and Eddy-Driven Jet Position and Their Response to Warming, J. Clim., 32, 1151–1166, https://doi.org/10.1175/JCLI-D-18-0434.1, 2019.

Weltje, G. J.: Quantitative analysis of detrital modes: statistically rigorous confidence regions in ternary diagrams and their use in sedimentary petrology, Earth-Sci. Rev., 57, 211–253, https://doi.org/10.1016/S0012-8252(01)00076-9, 2002.

Weltje, G. J., Van Ansenwoude, S. O. K. J., and de Boer, P. L.: High-frequency detrital signals in Eocene fan-delta sandstones of mixed parentage (south-central Pyrenees, Spain); a reconstruction of chemical weathering in transit, J. Sediment. Res., 66, 119–131, https://doi.org/10.1306/D42682CF-2B26-11D7-8648000102C1865D, 1996.

Werner, C., Schmid, M., Ehlers, T. A., Fuentes-Espoz, J. P., Steinkamp, J., Forrest, M., Liakka, J., Maldonado, A., and Hickler, T.: Effect of changing vegetation and precipitation on denudation – Part 1: Predicted vegetation composition and cover over the last 21 thousand years along the Coastal Cordillera of Chile, Earth Surf. Dyn., 6, 829–858, https://doi.org/10.5194/esurf-6-829-2018, 2018.

Wiedicke-Hombach, M. and Shipboard Scientific Party: Cruise Report SO161-5 SPOC (Subduction Processes off Chile). Geologye Geochemistry-Heatflow, Hannover., 2002.

Wodzicki, K. R. and Rapp, A. D.: Variations in Precipitating Convective Feature Populations with ITCZ Width in the Pacific Ocean, J. Clim., 33, 4391–4401, https://doi.org/10.1175/JCLI-D-19-0689.1, 2020.

Yeh, S.-W., Cai, W., Min, S.-K., McPhaden, M. J., Dommenget, D., Dewitte, B., Collins, M., Ashok, K., An, S.-I., Yim, B.-Y., and Kug, J.-S.: ENSO Atmospheric Teleconnections and Their Response to Greenhouse Gas Forcing, Rev. Geophys., 56, 185–206, https://doi.org/10.1002/2017RG000568, 2018.

Yuan, S., Chiang, H.-W., Liu, G., Bijaksana, S., He, S., Jiang, X., Imran, A. M., Wicaksono, S. A., and Wang, X.: The strength, position, and width changes of the intertropical convergence zone since the Last Glacial Maximum, Proc. Natl. Acad. Sci., 120, e2217064120, https://doi.org/10.1073/pnas.2217064120, 2023.

Yuan, X., Kaplan, M. R., and Cane, M. A.: The Interconnected Global Climate System—A Review of Tropical–Polar Teleconnections, J. Clim., 31, 5765–5792, https://doi.org/10.1175/JCLI-D-16-0637.1, 2018.

Zech, R., Kull, C., Kubik, P. W., and Veit, H.: Exposure dating of Late Glacial and pre-LGM moraines in the Cordon de Doña Rosa, Northern/Central Chile (~31° S), Clim. Past, 3, 1–14, https://doi.org/10.5194/cp-3-1-2007, 2007.

Zhang, C., Huang, G., Yan, D., Wang, H., Zeng, G., Wang, S., and Li, Y.: Analysis of South American climate and teleconnection indices, J. Contam. Hydrol., 244, 103915, https://doi.org/10.1016/j.jconhyd.2021.103915, 2022.

Zhang, Y., Wallace, J. M., and Battisti, D. S.: ENSO-like Interdecadal Variability: 1900–93, J. Clim., 10, 1004–1020, https://doi.org/10.1175/1520-0442(1997)010<1004:ELIV>2.0.CO;2, 1997.